A single-column model intercomparison on the stratocumulus representation in present-day and future climate

S Dal Gesso, J.J. van Der Dussen, A.P. Siebesma, S.R. de Roode, I.A. Boutle, Y Kamae, R Roehrig, J Vial

RESEARCH ARTICLE

Correspondence to:
S. Dal Gesso,
gesso@knmi.nl

A single-column model intercomparison on the stratocumulus representation in present-day and future climate

S. Dal Gesso[1], J. J. van der Dussen[2], A. P. Siebesma[1,2], S. R. de Roode[2], I. A. Boutle[3], Y. Kamae[4], R. Roehrig[5], and J. Vial[6]

[1]Global Climate Division, Royal Netherlands Meteorological Society (KNMI), De Bilt, Netherlands, [2]Department of Geoscience and Remote Sensing, Delft University of Technology, Delft, Netherlands, [3]Met Office, Exeter, UK, [4]Center for Global Environmental Research, National Institute for Environmental Studies, Tsukuba, Japan, [5]CNRM-GAME, Meteo-France and CNRS, Toulouse, France, [6]Laboratoire de Meteorologie Dynamique, Centre National de la Recherche Scientifique and Universite Pierre et Marie Curie, Paris, France

Abstract Six Single-Column Model (SCM) versions of climate models are evaluated on the basis of their representation of the dependence of the stratocumulus-topped boundary layer regime on the free tropospheric thermodynamic conditions. The study includes two idealized experiments corresponding to the present-day and future climate conditions in order to estimate the low-cloud feedback. Large-Eddy Simulation (LES) results are used as a benchmark and GCM outputs are included to assess whether the SCM results are representative of their 3-D counterparts. The SCMs present a variety of dependencies of the cloud regime on the free tropospheric conditions but, at the same time, several common biases. For all the SCMs the stratocumulus-topped boundary layer is too shallow, too cool, and too moist as compared to the LES results. Moreover, they present a lack of clouds and liquid water and an excess of precipitation. The disagreement among SCMs is even more distinct for the response to a climate perturbation. Even though the overall feedback is positive for all the models, in line with the LES results, the SCMs show a rather noisy behavior, which depends irregularly on the free tropospheric conditions. Finally, the comparison with the host GCM outputs demonstrates that the considered approach is promising but needs to be further generalized for the SCMs to fully capture the behavior of their 3-D counterparts.

1. Introduction

Marine boundary layer clouds strongly affect the energy budget of the planet. Their primary effect is to enhance the planetary albedo. This is particularly effective for the persistent fields of stratocumulus (Scu) that are found over the eastern basins of the subtropical oceans. The Scu clouds form in high-pressure regions, over relatively cold water. Their cloud cover and optical thickness result from the delicate interaction between the large-scale conditions, the turbulent and convective mixing, and the microphysical processes. Changes in the cloud properties, as a result of a climate change, might lead to a response that can even offset the global temperature increase [*Randall et al.*, 1984].

In Global Circulation Models (GCMs), clouds are not explicitly resolved but are the result of a suite of physical parameterizations. Several studies have shown that the representation of Scu in GCMs is affected by enduring biases [e.g., *Webb et al.*, 2001; *Nam et al.*, 2012]. Furthermore, it has been found that the main source of uncertainties in future climate predictions is the low-cloud feedback [*Bony and Dufresne*, 2005; *Vial et al.*, 2013] and that Scu clouds contribute the most to the intermodel spread [*Williams and Webb*, 2009].

To tackle this problem it is necessary to gain insight in the mechanisms that control the Scu response to changes in the large-scale conditions. To this end, CGILS (CFMIP-GASS Intercomparison of Large-Eddy Simulations (LES) and Single Column Models (SCM), where CFMIP stands for Cloud Feedback Model Intercomparison Project and GASS for Global System Atmospheric Studies) has been set up [*Zhang and Bretherton*, 2008]. The experimental design includes three cases corresponding to three cloud regimes: well-mixed Scu, decoupled Scu, and cumulus (Cu). For each case the models have been forced by idealized large-scale conditions representing the present-day and the future climate conditions. The equilibrium states of these two experiments have been compared to estimate the cloud response to such a perturbation. The LES models

give a consistent response for all the cloud regimes, whereas the SCMs present a large spread both in the sign and in the magnitude of the feedback [*Zhang et al.*, 2013; *Blossey et al.*, 2013].

With the intent of generalizing the CGILS project, *Dal Gesso et al.* [2014a] designed a framework for studying the Scu equilibrium states dependency on the free tropospheric conditions, for present-day and future climate. The framework has been successfully employed in a Mixed-Layer Model (MLM), in a SCM, and in a LES study [*Dal Gesso et al.*, 2014a, 2014b; *van der Dussen et al.*, 2014, respectively]. These studies lay the basis for the present work which adopts the same framework and a complete hierarchy of models. A LES model is used as a benchmark to evaluate several SCMs. Subsequently, GCM outputs are analyzed with a similar approach, to assess the correspondence with the SCM's 3-D counterparts.

The experimental setup is summarized in section 2 and the considered models are described in section 3. The SCM representation of the Scu dependence on the free tropospheric conditions is evaluated in section 4. The Scu response to a perturbation in the large-scale forcing is discussed in section 5. Finally a summary of the most important conclusions is reported in section 6.

2. Experimental Design

2.1. Control Climate Experiment
The experimental setup adopted in the present work has been presented first in *Dal Gesso et al.* [2014a] and then in *Dal Gesso et al.* [2014b]. In this section, we will briefly summarize the general design and for a more detailed description we refer to *Dal Gesso et al.* [2014b].

This study aims to evaluate SCMs on the basis of their representation of the dependence of the cloud regime on the free tropospheric conditions. To this end the setup entails several experiments that only differ in the free tropospheric thermodynamic profiles. The different cases are identified by the contrast between the free tropospheric and the surface conditions in temperature and in humidity through the bulk jumps defined as

$$LTS = \theta_{700} - \theta_0$$
$$\Delta q_t = q_{t,700} - q_{t,0},$$

(1)

where θ is the potential temperature and q_t is the total specific humidity. The subscript 700 and 0 denote the values at 700 hPa and at the surface, respectively. The lower tropospheric stability (LTS) was introduced by *Klein and Hartmann* [1993] and has been widely used as a predictor of the cloud coverage. The latter is a similar measure but for humidity and it has been defined for the first time in *Dal Gesso et al.* [2014a]. In the present study the considered free tropospheric conditions correspond to the following ranges:

$$LTS = [17, 26]K; \quad \Delta q_t = [-10, -5]\text{g kg}^{-1},$$

with a step of 0.5 K and 0.5 g kg^{-1}, respectively. *Dal Gesso et al.* [2014a] verified that these ranges are representative of the Scu region in the North-East Pacific, off the coast of California, for the considered large-scale conditions.

For all cases the boundary layer is initialized as vertically well mixed and totally overcast. It is capped by a strong inversion, above which the free tropospheric temperature follows a moist adiabatic lapse rate and the free tropospheric humidity is constant up to 3 km, above which it decreases exponentially. The temperature profile in the upper atmosphere is identical for all the cases. Above 3 km, the temperature and humidity profiles are nudged toward the initial conditions.

The large-scale forcings are set consistently to the CGILS experiment corresponding to the decoupled Scu regime. The sea surface temperature (SST) is 292 K for all the cases. The wind velocity components are set equal to the geostrophic wind components, U_g and V_g, which are constant with height. The large-scale horizontal advection of temperature and humidity are not considered. In order to avoid oscillations due to the diurnal cycle, the zenith angle is set constant and equal to the diurnally averaged value as in *Zhang and Bretherton* [2008]. Details on the vertical profiles of T and q_t are reported in *Dal Gesso et al.* [2014b] (Table 1).

The setup comprises two experiments one with a subsidence which is constant in time and a second one which includes an additional stochastic noise. In the upcoming sections the experiments will be labeled as *constant forcing (C.F.)* and *stochastic forcing (S.F.)* experiment, respectively. The mean profile of the subsidence, $\bar{w}(z)$, is defined as

Table 1. Participating Models (in Brackets a Shorter Version of the Name, Used Hereafter, is Reported), Institutions, and Scientists[a]

Model Acronym	Institution	Scientists	Reference	Vertical Levels (<1 km)
EC-EARTH	KNMI (Royal Netherlands Meteorological Institute)	S. Dal Gesso, A. P. Siebesma	*Hazeleger et al.* [2012]	63 (12)
HadGEM2, Hadley Centre Global Environmental Model version 2	Met Office, UK	I. A. Boutle	*Martin et al.* [2011]	38 (7)
HadGEM3-GA3.0 (HadGEM3), Hadley Centre Global Environmental Model version 3	Met Office, UK	I. A. Boutle	*Walters et al.* [2011]	63 (11)
IPSL-CM5A-LR (IPSL), Institut Pierre Simon Laplace, climate model version 5A, low resolution4	IPSL (Institute Pierre-Simone Laplace), France	J. Vial	*Hourdin et al.* [2006]	39 (7)
CNRM-CM5 (CNRM), Centre National De Recherches Meteorologiques, Climate Model version 5	Meteo France	R. Roehrig	*Voldoire et al.* [2013]	31 (5)
MIROC5 (MIROC), Model for Interdisciplinary Research On Climate version 5	NIES (National Centre for Environmental Studies), Japan	Y. Kamae, M. Watanabe	*Watanabe et al.* [2010]	40 (11)
DALES 4.0 (DALES), Dutch Atmospheric Large-Eddy Simulation	TU Delft (Delft University of Technology)	J. J. van der Dussen, S.R. de Roode	*Heus et al.* [2010] and *Böing et al.* [2012]	−(100)

[a]The main references and the number of vertical levels in the whole atmospheric column as well as in the first kilometer of atmosphere are reported.

$$\bar{w}(z) = w_0(1 - e^{-\frac{z}{z_w}}), \qquad (2)$$

where w_0 is an asymptotic value and z_w is a length scale [*Bellon and Stevens*, 2012]. As such, the subsidence warming balances the radiative cooling above 2 km, for all the considered cases. In the second experiment a stochastic component is included so that the subsidence is defined as

$$w(z, t) = \bar{w}(z) + \bar{w}(z) \cdot X(t), \qquad (3)$$

where X is a random number that is defined within the range between δ_w and $-\delta_w$, with $\delta_w = 0.5$, every 6 h [*Cheedela*, 2013; *Dal Gesso et al.*, 2014b]. It is worth mentioning that there is no correlation in time for the random numbers; thus, they are independent of each other. This method has been applied for the first time by *Brient and Bony* [2012] to account for the natural variability of the large-scale vertical velocity. Only in this way there was a correspondence between the vertical structure obtained with a GCM and the SCM counterpart. Following this idea, *Dal Gesso et al.* [2014b] included an experiment with an additional stochastic noise defined as in (3), in a SCM study. It was demonstrated that this strategy is valuable to limit the dependence of the results on the initial conditions and on the vertical resolution.

2.2. Perturbed Climate Experiment

In order to assess the effect of a perturbation in the large-scale forcing on the SCM equilibria, the SST is increased by 2 K. A uniform warming of the troposphere is imposed as in *Rieck et al.* [2012] such that the LTS does not change. Furthermore, the initial humidity profile is increased as to maintain the relative humidity (RH) as in the control climate experiment. As the change in Δq_t is governed by the Clausius-Clapeyron relation, the bulk jump is enlarged, though the cases are identified by the values of LTS and Δq_t of the control case. The wind velocity and the subsidence are not perturbed. Also, for the perturbed climate experiment, both a subsidence which is constant in time and a subsidence with an additional stochastic noise are considered.

The considered climate perturbation is a simplified version of the climate change obtained by state of the art GCMs. It does not include the decrease in both the subsidence and the horizontal wind velocity, due to the weakening of the Hadley circulation [e.g., *Vecchi et al.*, 2006]. Moreover, a strengthening of LTS is expected because of the steepening of the adiabatic lapse rate [*Qu et al.*, 2013]. In this sense, the perturbed climate experiment does not correspond directly to the local effect of climate warming.

Table 2. Main References of the Most Important Parameterizations Involved in the Representation of the Scu-Topped Boundary Layer[a]

Model	PBL Scheme	Shallow Convection Scheme	Cloud Scheme	Microphysics Scheme
EC-EARTH	*Siebesma et al.* [2007] (CTE)	*Tiedtke* [1989]	*Tiedtke* [1993]	*Tiedtke* [1993]
HadGEM2	*Lock et al.* [2000] (CTE)	*Grant* [2001]	*Smith* [1990]	*Wilson and Ballard* [1999]
HadGEM3	*Lock et al.* [2000] (CTE)	*Grant* [2001]	*Wilson et al.* [2008]	*Wilson and Ballard* [1999]
IPSL	*Deardorff* [1966]	*Emanuel* [1991]	*Bony and Emanuel* [2001]	*Bony and Emanuel* [2001]
CNRM	*Mellor and Yamada* [1974]	×	*Ricard and Royer* [1993]	*Kessler* [1995]
MIROC	*Nakanishi and Niino* [2004]	×	*Watanabe et al.* [2009]	*Wilson and Ballard* [1999]

[a]For the PBL scheme the explicit representation of the entrainment flux at the cloud top is indicated by the label "CTE" (i.e., cloud top entrainment). A cross is used when a SCM does not include one of the considered parameterizations and the other parameterizations represent the corresponding physical process.

3. Description of the Models

3.1. Single-Column Models Description

The present model intercomparison study includes six SCMs. A list of the model acronyms, the main references, and the scientists participating in this project is reported in Table 1. The GCM counterparts of five SCMs participated in the Coupled Model Intercomparison Project version 5 (CMIP5), while HadGEM3 is the climate model being developed at the Met Office for CMIP6. The SCMs are run in the operational setting; thus, they present a variety of vertical resolutions. The number of vertical levels in the whole atmospheric column and in the first kilometer is reported in Table 1. The time step differs from model to model but this model feature is not reported as the data are provided as six-hourly averages. The choice of this time interval is motivated by the definition of the stochastic component of the subsidence. To account for possible fluctuations due to the vertical resolution and the interaction between different parameterizations, as found in *Zhang and Bretherton* [2008], the SCMs are run for 100 days.

The Scu-topped boundary layer representation in a SCM depends primarily on the parameterizations involved in the turbulent and convective mixing within the boundary layer and on the calculation of the cloud fraction and liquid water content. In this sense the relevant parameterizations for this study are the boundary layer (PBL), the convection, the cloud scheme, and the microphysics scheme. The main references for the schemes used in the participating SCMs are listed in Table 2. Moreover, it is indicated whether the PBL scheme includes an explicit term to account for entrainment at the cloud top.

3.2. Global-Circulation Model Output

The SCM results are compared to the outputs of the host GCMs. Within the CMIP5 data set [*Taylor et al.*, 2012], results from the AMIP experiment are explored. For this experiment the models are run in an atmosphere-only mode, with prescribed SSTs. The most similar future climate scenario to the investigated climate perturbation corresponds to a uniform increase of SST by 4 K, as imposed in the AMIP4K experiment. Monthly means are available for the period 1979–2008 for the 3-D counterparts of all the considered SCMs except HadGEM3. Only the subtropical regions dominated by marine Scu are included in the analysis and Table 3 shows their locations [*Klein and Hartmann*, 1993].

3.3. DALES Specifications

The results of the Dutch Atmospheric LES (DALES) are used as a benchmark in this study. For a detailed description of the LESs presented in this article, we refer to a companion article by *van der Dussen et al.* [2014]. The simulations are run for 10 days on a domain consisting of 120 points in each direction, spaced 50 m apart. The vertical grid consists of 219 levels with a resolution of 10 m up to a height of 2 km. The top of the domain is at 3 km and at that height the values of θ_l and q_t are kept constant to mimic the nudging applied in the SCM simulations.

Table 3. Locations of the Considered Subtropical Regions Dominated by Marine Scu [*Klein and Hartmann*, 1993]

Subtropical Scu Regions		
California	20°N–30°N	120°–130°W
Canary Islands	15°N–25°N	25°E–35°E
Perù	10°S–20°S	80°–90°W
Namibia	10°S–20°S	0°E–10°E

4. Control Climate Results

4.1. LES Results

As an example, the LES results for the case located at the center of the phase space are examined. Figure 1 displays the time evolution of the cloud fraction and the mean vertical profiles of θ_l and q_t, where θ_l is the liquid water potential temperature. Hereafter, we define the mean state of the LES results as the average over the last day of simulation.
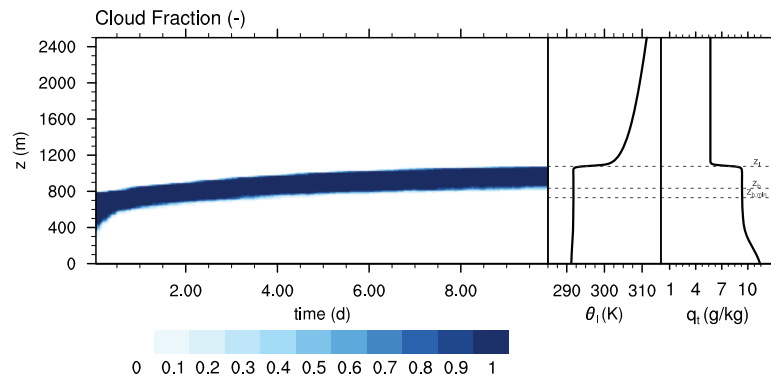
Figure 1. DALES results for the case located at the center of the phase space: time evolution of the cloud fraction and mean vertical profiles of θ_l and q_t. In the right figures the cloud top height (z_i), the cloud base height (z_b) and the minimum cloud base height ($z_{b,min}$) are shown.

The boundary layer deepens until reaching an equilibrium. For the whole simulation time the boundary layer remains overcast. The mean vertical profile of θ_l is vertically well mixed within the boundary layer and is capped by a strong inversion as expected for Scu-topped boundary layers [e.g., *Wood*, 2012]. The q_t profile appears to be less well mixed. It is constant with height in the upper part of the boundary layer and decreases with height close to the surface. This vertical structure can be loosely defined as a *decoupled boundary layer*. As the incoming radiative flux at the top of the atmosphere is set equal to the daily mean, the thermodynamic vertical profiles can be interpreted as an average between daytime and nighttime conditions. During the night the Scu-topped boundary layer is generally well-mixed, while during the day the effect of the solar radiation tends to destabilize the system leading to a two-layer structure typical of a decoupled boundary layer.

The goal of the present work is to study the dependence of the cloud regime on the free tropospheric conditions. To this end, in the upcoming sections we will mainly focus on the liquid water path (LWP) and the total cloud cover (TCC). Figure 2 displays the mean state of TCC and LWP in the phase space defined by (1). For computational reasons the results of only a subset of the considered cases are available. The TCC shows no variation and the boundary layer is totally overcast for all the considered cases (Figure 2a). The LWP is almost independent of the LTS, while it presents a strong dependence on Δq_t with a net increase for moister free tropospheric conditions.

To better understand the LWP pattern in the phase space, we extend the analysis to the cloud top height (z_i), the cloud base height (z_b), the vertically averaged value of q_t and θ_l in the boundary layer ($\langle q_t \rangle$ and $\langle \theta_l \rangle$), i.e., between z_i and the surface, and the surface fluxes, namely the latent heat flux (LHF) and the sensible heat flux (SHF). The cloud base height is defined as the slab average of the lowest height at which the cloud cover is nonzero. As a first-order approximation, we use a multiple linear regression procedure to describe the variation of a variable, ψ, as a function of LTS and Δq_t

$$\psi \approx b_0 + b_1 \cdot LTS + b_2 \cdot \Delta q_t + \varepsilon, \tag{4}$$

where b_0, b_1, and b_2 are the regression coefficients and ε is the standard error of the regression which is estimated as

$$\varepsilon = \sqrt{\frac{\sum_{i=0}^{N_i} \sum_{j=0}^{N_j} [\psi_{i,j} - (b_0 + b_1 \cdot LTS_i + b_2 \cdot \Delta q_{t,j})]^2}{\nu}}, \tag{5}$$

where ν is the number of degrees of freedom which is the number of cases minus 3. The subscripts i and j are the indices which indicate the LTS and Δq_t identifying each experiment. Therefore, the number of cases is $N_i \cdot N_j$, as N_i and N_j are the numbers of considered LTS and Δq_t, respectively. To directly compare the contribution of LTS with the contribution of Δq_t, the regression coefficients are normalized by the standard deviations within the phase space, σ, where the subscript indicates the variable on which it is applied

$$B_1 = b_1 \frac{\sigma_{LTS}}{\sigma_\psi}$$
$$B_2 = b_2 \frac{\sigma_{\Delta q_t}}{\sigma_\psi}. \tag{6}$$

The main focus will be on b_1 and b_2 (B_1 and B_2), as the aim of this analysis is to describe the qualitative dependence on the free tropospheric conditions.
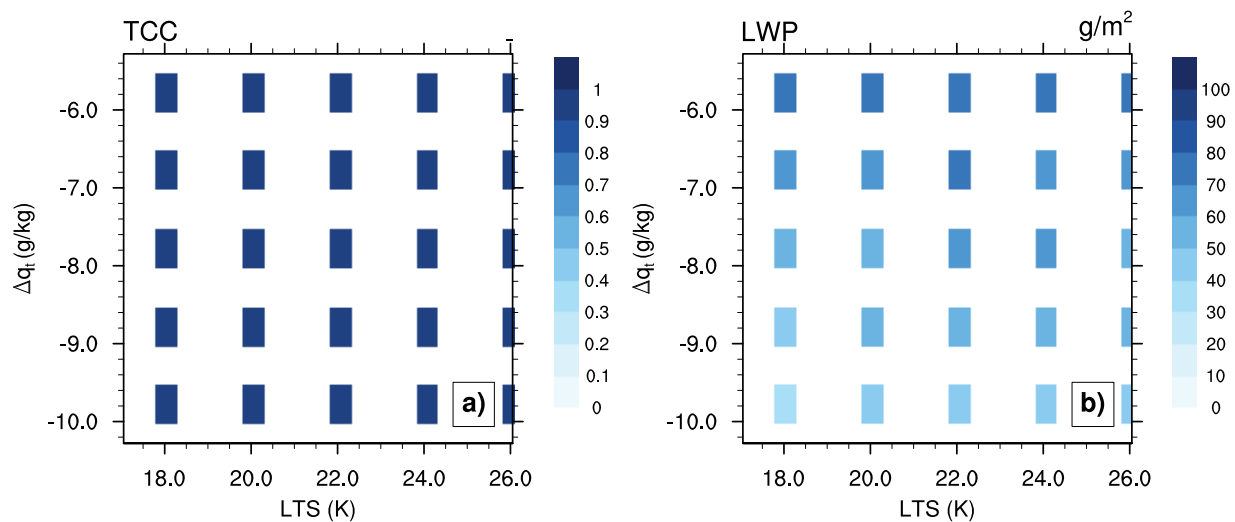
Figure 2. DALES results of the mean states of the total cloud cover (TCC) and the liquid water path (LWP).

Tables A3–A8 (collected in the Appendix A) collect the multiple linear regression coefficients and the standard errors of z_i, z_b, $\langle q_t \rangle$, $\langle \theta_l \rangle$, LHF, and SHF, respectively. The standard error is rather small for all the considered variables with respect to the overall averages in the phase space reported in Table 4; thus, the approximation is fairly good. A cooler and drier free troposphere supports a higher z_i and z_b. A weaker thermal stratification at the cloud top and a weaker long-wave radiative flux in the free troposphere lead to an increase in the entrainment rate. As a consequence, the boundary layer deepens and, at the same time, becomes drier and warmer, leading to a z_b increase. The surface fluxes strongly depend on one of the two bulk jumps: the LHF on Δq_t and the SHF on LTS. Note that the SHF presents very small and negative values in the whole phase space (not shown).

It is worth comparing the LES results with the MLM results reported in *Dal Gesso et al.* [2014a]. As already mentioned the LES vertical profiles of the conserved variables θ_l and q_t show a double-layer structure, while the MLM framework assumes a constant value in the boundary layer for those variables. Qualitatively the dependence of z_i, z_b, $\langle \theta_l \rangle$, and $\langle q_t \rangle$ is consistent between the two models. However, the LWP pattern is substantially different as the MLM predicts a cloud thickening toward cooler and drier free tropospheric conditions. This is due to the combined effects of the lack of decoupling in the MLM solutions and the simplified radiation parameterization used in that study. Due to the well-mixedness hypothesis the LWP presents a stronger dependence on LTS as compared to DALES results [*Bretherton et al.*, 2013]. At the same time, a too strong variance of the long-wave (LW) cooling in the phase space causes large variations of $\langle \theta_l \rangle$, which directly affects the LWP pattern.

4.2. SCM Results
4.2.1. Time Evolution of a Prototype Case
Similarly to Figure 1, the SCM results for the case located at the center of the phase space are displayed in Figure 3, for both the experiment with a constant subsidence in time (left column) and with an additional stochastic noise (right column). The time evolution of the cloud fraction is presented together with the mean states of the vertical profiles of θ_l and q_t. Due to the coarse vertical resolution and the interaction of the different physical parameterizations, the SCMs present two types of equilibria, either a stationary equilibrium, which is constant in time, or a fluctuating equilibrium, when the cloud layer fluctuates between different levels. The introduction of a stochastic component in the large-scale subsidence is expected to result in more likely fluctuating equilibria. In order to take into account these considerations we define the mean state for the SCM results as the average in time over the last 80 days of simulation. Note that Figure 3 is intended to be a sanity check to assess whether the models achieve an equilibrium and the free tropospheric thermodynamic conditions correspond to the initialization.

The majority of the models reaches a stationary equilibrium when forced by a constant subsidence; only HadGEM3 and MIROC present a fluctuating equilibrium. The response to the additional stochastic noise is

Table 4. Average and Standard Deviation Within the Phase Space of the LES Results

DALES—Overall Results		
LWP	(g m^{-2})	59.63 ± 12.16
z_i	(m)	1097 ± 285
z_b	(m)	635 ± 238
$\langle q_t \rangle$	(g kg^{-1})	9.74 ± 1.049
$\langle \theta_l \rangle$	(K)	291.62 ± 0.12
LHF	(W m^2)	41.97 ± 9.59
SHF	(W·m^2)	−2.16 ± 0.75

rather limited for several models (EC-EARTH, CNRM, and IPSL). HadGEM2 shows a stationary equilibrium in the constant forcing experiment and a fluctuating equilibrium in the stochastic forcing experiment. Furthermore, the free tropospheric conditions are in general not different from the initial profiles, except for CNRM and MIROC. MIROC presents spurious fluctuations in the q_t profile, leading to sudden condensation above the boundary layer (see Figures 3m and 3n). The free tropospheric profile of q_t obtained with CNRM (Figures 3i and 3l) shows an overshoot right above the inversion. In the boundary layer the models are generally rather well-mixed. The two-layer structure discussed for the LES results is clearly not found for any of the SCMs.

4.2.2. Simulated Cloud Regime

All the considered cases are analyzed in the phase space defined by (1). The mean states of the TCC (Figure 4) and LWP (Figure 5) are examined for both the experiment with a constant subsidence (left column) and an additional stochastic noise (right column). For some cases corresponding to humid and cool free tropospheric conditions (upper left corner of the phase space), a cloud layer forms above 3 km because of the generation of energetic plumes. HadGEM2, HadGEM3, IPSL, and CNRM present this feature. As the presence of a high-level cloud layer above the Scu-topped boundary layer is beyond the interest of this article, those cases are excluded from our analysis.

The patterns of TCC (Figure 4) in the phase space differ noticeably from model to model. However, the model fingerprint is rather distinct and is not strongly affected by the additional stochastic noise added to the subsidence. EC-EARTH (Figures 4a and 4b), HadGEM2 (Figures 4c and 4d), and CNRM (Figures 4i and 4l) present a fairly constant TCC = 1 in a large area of the phase space, consistent with the LES results. A TCC reduction is found in the lower left corner of the phase space. IPSL exhibits a constant TCC in the phase space but the value is lower than in the LES results (Figures 4g and 4h). MIROC shows a net increase in the TCC toward weaker LTS and moister free tropospheric conditions (Figures 4m and 4n). A similar behavior is found for HadGEM3, though for different reasons. In fact, HadGEM3 presents a wide region of the phase space, corresponding to stronger LTSs, with TCC lower than 10% (Figures 4e and 4f). For these cases the cloud layer slowly dissolves and once the boundary layer becomes clear it warms quickly and becomes stably stratified. In absence of the horizontal advection of cold or moist air, the cloud layer cannot reform again. Sensitivity studies (not shown) clarified that the cloud scheme is responsible for this extreme behavior. When replaced by the scheme used in the older version of the model such a massive cloud loss is not found (for references see Table 2).

The mean states of LWP are displayed in Figure 5. The spread among the models is even more distinct than for the TCC patterns. Also, for this quantity the model fingerprint is not strongly affected by the stochastic noise added to the subsidence. None of the SCMs completely capture the LWP dependence on the free tropospheric conditions found in the LES results. More precisely they collectively fail to exhibit a decrease of LWP with increasing Δq_t. EC-EARTH (Figures 5a and 5b) and HadGEM2 (Figures 5c and 5d) exhibit a LWP increase for a weaker LTS and a drier free troposphere in the region of the phase space corresponding to a totally overcast boundary layer. The abrupt decrease in LWP in the lower left corner of the phase space corresponds to a TCC reduction. HadGEM3 shows a net increase in LWP toward weaker LTSs due to the wide region corresponding to the clear-sky regime (Figures 5e and 5f). A rather constant pattern is shown by IPSL (Figures 5g and 5h). For CNRM the only noticeable variation is found in the lower left corner and corresponds to a cloud breakup due to the selected color scale (Figures 5i and 5l). Actually, in the region corresponding to a totally overcast boundary layer, the LWP depends mainly on LTS and increases for a weaker LTS (Table 2). Similar to CNRM, MIROC presents a LWP pattern which is almost independent of Δq_t and increases for a weaker LTS (Figures 5m and 5n).

It is worth mentioning that in *Dal Gesso et al.* [2014b] larger differences between the results obtained with a constant subsidence in time and one including an additional stochastic noise were found. The study was conducted with the SCM version of EC-EARTH but with a higher-resolution grid. The results suggest that the considered noise might be too weak to strongly affect the patterns because of the coarse vertical resolutions that are used here.
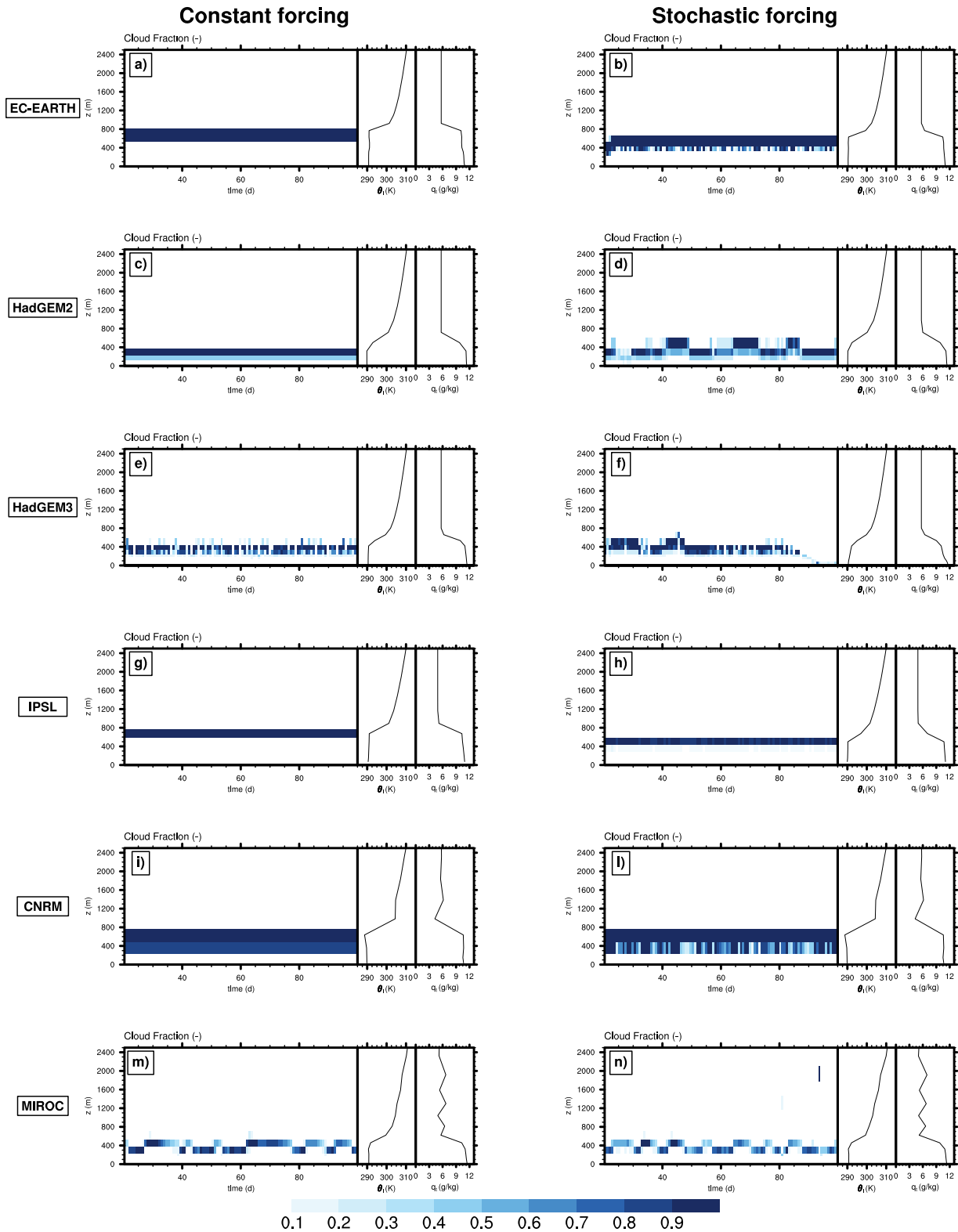
Figure 3. Same as Figure 1, but for all the considered SCMs. The results of the (right) constant forcing experiment and (right) stochastic forcing experiment.

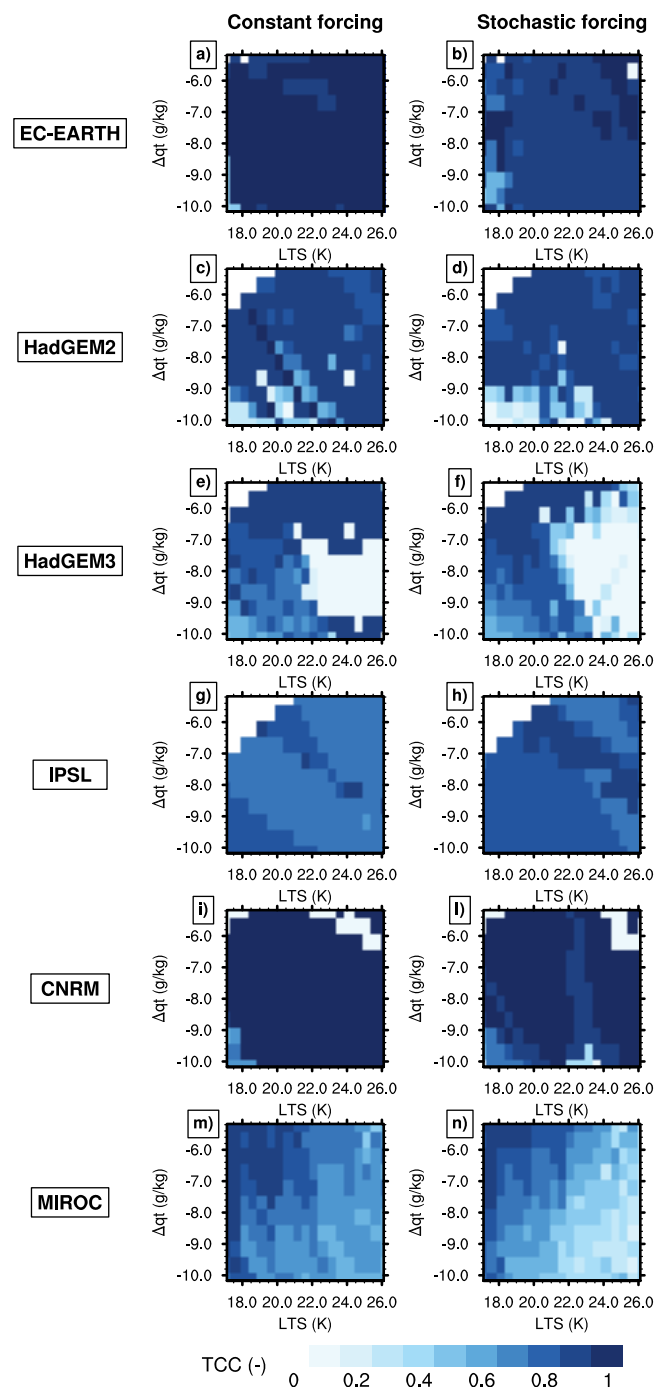**Constant forcing**   **Stochastic forcing**

Figure 4. Mean state of the TCC of all the considered SCMs. The results of the (left) constant forcing experiment and (right) stochastic forcing experiment.

4.2.3. Boundary Layer Mean State

To extend the analysis, a multiple linear regression is applied to z_i, z_b, the boundary layer averages of q_t and θ_l, $\langle q_t \rangle$ and $\langle \theta_l \rangle$, LHF, and SHF and the results are collected in Tables (A1–A8), respectively. The cloud top height is defined as the highest level with a cloud fraction greater than zero and the cloud base corresponds to the lowest cloudy level.

First of all the sign of the regression coefficients generally do not change between the two experiments, whereas the relative importance of LTS and Δq_t might change. The standard error of the regression, ε, is larger than for the LES results. This is due to the noisy patterns generally obtained with the SCMs. As a sanity check for the applicability of the method the linear regression coefficients of TCC (Table 1) and LWP (Table 2) are reported. The patterns discussed in the previous section are well described by the regression coefficients. Therefore, a multiple linear regression is a good approximation also for SCM results.

The representation of the dependence of z_i and z_b on the free tropospheric conditions is fairly good for all the models as compared to the LES results (Tables 3 and 4). The boundary layer becomes deeper and the cloud base raises for cooler and drier free tropospheric conditions. However, in general the models show a stronger dependence of both z_i and z_b on LTS with respect to Δq_t (EC-EARTH, HadGEM2, HadGEM3, and MIROC). All the SCMs agree on the dependence of $\langle q_t \rangle$ on the bulk jumps (Table 5). Consistent with the LES results, the boundary layer

becomes drier for a weaker LTS and a drier free troposphere. Furthermore, EC-EARTH, HadGEM2, IPSL, and CNRM capture the main dependence of $\langle q_t \rangle$ on Δq_t found in the LES results. None of the models completely capture the LES variation of $\langle \theta_l \rangle$ in the phase space (Table 6). Generally $\langle \theta_l \rangle$ mainly depends on Δq_t: all the SCMs present a boundary layer warming for a moister free troposphere for which there is a less intense radiative cooling at the cloud top. For EC-EARTH, HadGEM2, and MIROC the boundary layer is found to become warmer for a weaker LTS as more free tropospheric air can penetrate in the cloud layer, consistently with the LES results. IPSL and CNRM (only in the constant forcing experiment) present a decrease in $\langle \theta_l \rangle$ for
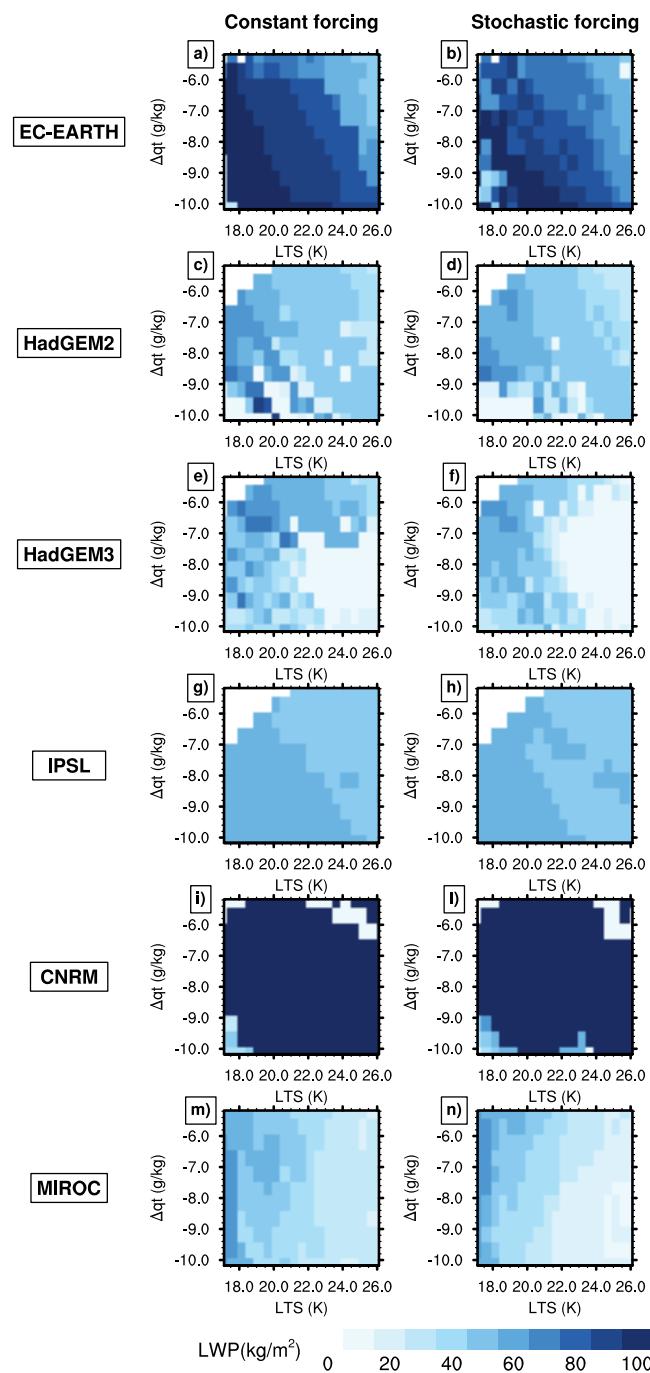
Figure 5. Same as Figure 4, but for LWP.

weaker LTSs due to a higher temperature above the inversion layer. IPSL and CNRM have the coarsest vertical resolutions and for this reason show very little variation in z_i. At the equilibrium the entrainment flux at the cloud top balances the subsidence. From this perspective the entrainment rate at the cloud top does not vary for these models; thus, $\langle \theta_l \rangle$ shows only a dependence on the free tropospheric temperature. The regression coefficients for the SHF do not compare well with the ones obtained from the LESs (Table A8). EC-EARTH, HadGEM2, IPSL, and CNRM represent correctly the main dependence of LHF on Δq_t, with a net increase for drier free tropospheric conditions (Table 7).

4.2.4. Cloud Vertical Structure

As an illustration of the representation of the vertical profiles of the cloud fraction, four cases are examined and displayed in Figure 6. In order to span the whole range of considered free tropospheric conditions the cases are located along the diagonal from the upper right corner toward the lower left corner. For visualizing the locations of these cases in the phase space we refer to the inset in the upper right corner of Figure 9. The previous analysis highlights that the results of the constant and stochastic forcing experiments are rather similar. Therefore, in the following sections we will mainly focus on the results obtained by adding a stochastic noise to the subsidence. This preference is motivated by previous studies which demonstrated that this strategy is valuable to avoid numerical artifacts and to have a more realistic forcing [*Brient and Bony*, 2012; *Dal Gesso et al.*, 2014b].

In general, the cloud top is located at a lower height in the SCMs than in the LES results. This is not only an effect of the vertical resolution as the cloud top height found in all the SCM results is not placed at the closest model level to the LES z_i, but several grid levels below. EC-EARTH (Figure 6a), HadGEM2 (Figure 6b), and CNRM (Figure 6e) capture fairly well the variation in the cloud structure for different free tropospheric conditions. For a stronger LTS and a moister free troposphere, they present a shallower boundary layer and the maximum cloud fraction is equal to unity or relatively high. A noticeable decrease in the cloud fraction is found for a weaker LTS and a drier free troposphere. HadGEM3 (Figure 6c) and MIROC (Figure 6f) present a boundary layer which deepens along the considered path but the maximum cloud fraction is rather low.
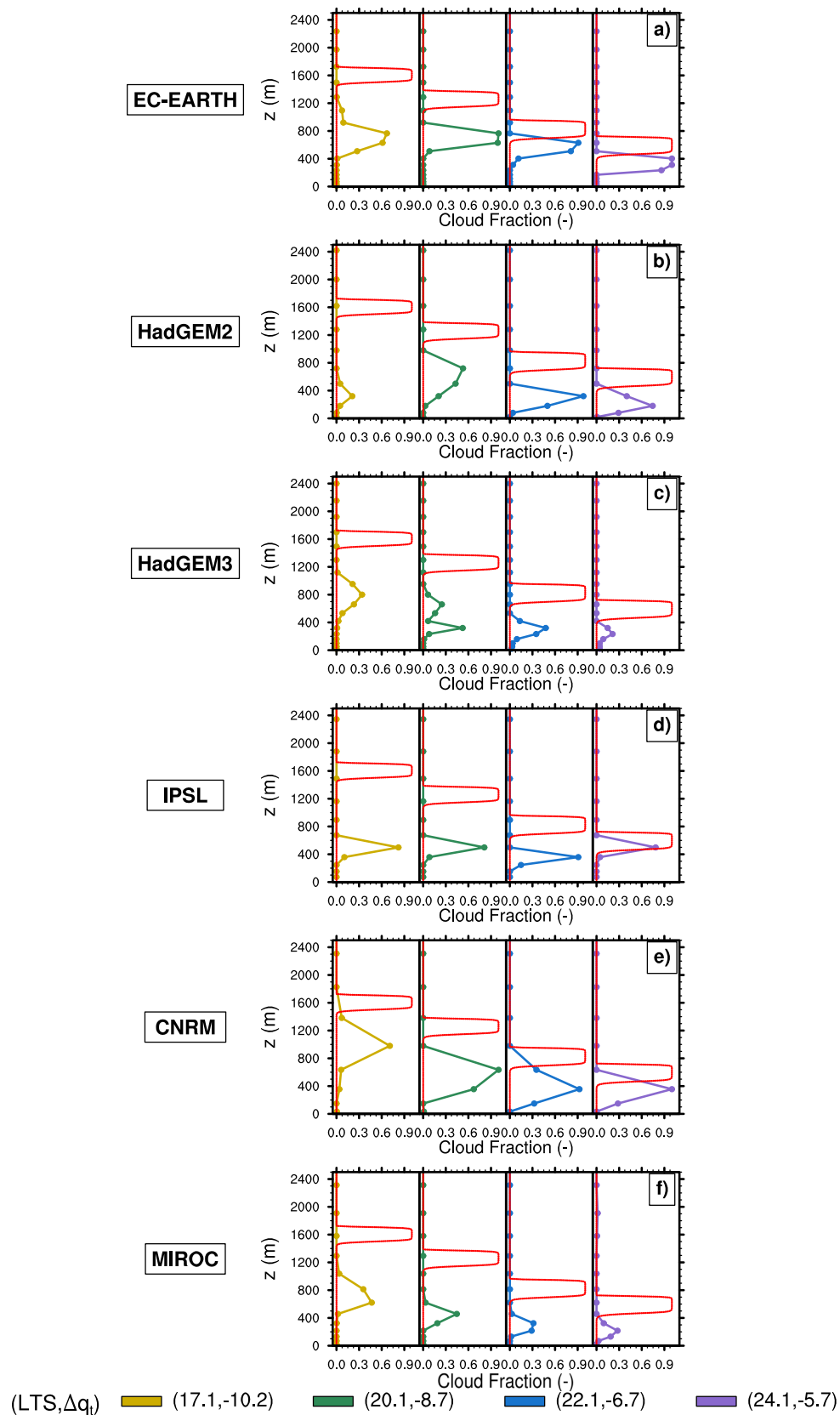
Figure 6. Mean state of the cloud fraction vertical profiles of all the considered SCMs. The SCM results are obtained by adding a stochastic noise to the subsidence. The markers indicate the SCM vertical grid levels. The LES results are depicted as the red lines.

Table 5. Mean Standard Deviation of TCC and LWP as Displayed in Figures 12 and 13, Respectively[a]

| Model | σ | |
	TCC (−)	LWP (g m^{-2})
EC-EARTH	0.12	14.3
HadGEM2	0.11	21.5
IPSL	0.10	13.4
CNRM	0.10	21.2
MIROC	0.08	14.5

[a]The values are calculated for each bin corresponding to a LTS-Δq_t combination and then averaged over the whole phase space.

Finally a rather constant structure is found for IPSL (Figures 6g and 6f). Consistent with the previous results, this model shows a weak dependence on the free tropospheric conditions.

4.2.5. Boundary Layer Structure

To further explore the internal structure of the boundary layer we will measure the level of decoupling through the decoupling parameter α_{q_t} introduced by *Park et al.* [2004]

$$\alpha_{q_t} = \frac{q_{t,CL} - q_{t,SC}}{q_{t,+} - q_{t,SC}},$$

where the subscripts CL and SC indicate the cloud and subcloud layer values which are calculated as the vertical average between z_i and z_b and between the minimum cloud base height ($z_{b,min}$) and the surface, respectively. As an illustration, the heights corresponding to z_i, z_b, and $z_{b,min}$ are highlighted in Figure 1. Lastly $q_{t,+}$ represents the condition above the inversion which depends on the case through Δq_t. To clarify, the higher the α_{q_t} values, the stronger the difference between the two layers becomes, the stronger the decoupling. A similar parameter can be defined as well for θ_l but we focus our analysis on the q_t profiles as the θ_l profiles are relatively well-mixed in the LES results. For the analysis of the SCM results we assume that the mean cloud base and the minimum cloud base coincides [*Dal Gesso et al.*, 2014b]. Our choice is motivated by the coarse vertical resolution and the shallow boundary layer which does not allow for this structure.

In addition to the comparison to the LES results, we will also consider a parameterization based on an observational study [*Park et al.*, 2004] which relates α_{q_t} to the difference between the cloud top height and $z_{b,min}$ as

$$\alpha_{q_t} = \left(\frac{z_i - z_{b,min}}{\Delta z_s}\right)^\gamma, \tag{7}$$

where $\Delta z_s = 2750m$ and $\gamma = 1.2$ are two scaling parameters. *Wood and Bretherton* [2004] have further tested this parameterization against observations and shown a strong correlation. The distance between z_i and $z_{b,min}$ is intended as a measure of the whole cloud layer, considering that for deep boundary layers, decoupling and the formation of cumuli underneath the Scu is expected [e.g., *Bretherton and Wyant*, 1997].

Figure 7 displays α_{q_t} as a function of $z_i - z_{b,min}$ for all the SCMs and for the LES results together with the parameterization (7). The clusters in the LES results show that α_{q_t} depends more strongly on LTS than Δq_t. The results show a large variety of regimes, ranging from a well-mixed Scu-topped boundary layer to a strongly decoupled Scu-topped boundary layer with penetrative cumuli underneath. The SCMs do not present the same variety as the LES, since they generally predict a shallow and well-mixed boundary layer. Actually all the SCMs but MIROC present lower values of α_{q_t} than expected from the parameterization introduced by *Park et al.* [2004]. However, the representation does not seem biased as the SCMs tend to predict a different regime with respect to DALES: a shallower, cooler, moister, and more well-mixed boundary layer. For such a boundary layer one would expect a TCC = 1 which is generally not found.

4.2.6. Model Ensemble Mean Results

We compute the model ensemble mean of the TCC and LWP mean states for the stochastic forcing experiment (Figure 8). The model ensemble mean results are in line with the previous findings: the TCC is lower than unity and the LWP dependence on the free tropospheric conditions is not consistent to the LES results. The LWP pattern shows a stronger dependence on LTS with respect to Δq_t, with a net increase for weaker LTSs, while the LWP pattern found with DALES presents a very strong dependence on Δq_t and is almost independent of LTS.

Similar to the previous analysis, the multiple linear regression coefficients are presented in Tables (A1–A8) for both

Table 6. Average and Standard Deviation Within the Phase Space of dCRE/dSST of All the SCM Results, C.F. and S.F. Indicate the Constant Forcing and Stochastic Forcing Experiment, Respectively

| Model | dCRE/dSST (W m^{-2} K^{-1}) | |
	C.F.	S.F.
EC-EARTH	0.46 ± 4.63	1.23 ± 8.57
HadGEM2	12.71 ± 23.37	11.95 ± 19.61
HadGEM3	13.69 ± 24.90	6.18 ± 17.04
IPSL	1.38 ± 1.45	1.34 ± 1.56
CNRM	10.14 ± 24.37	11.03 ± 28.65
MIROC	0.21 ± 2.30	0.34 ± 3.63
M.E.M.	6.27 ± 6.94	5.29 ± 7.05

Table 7. Same as Table 4 Except for the Responses to a Climate Perturbation

DALES—Overall Results		
dCRE/dSST	(W m^{-2} K^{-1})	7.95 ± 1.91
dLWP/dSST	(g m^{-2} K^{-1})	-6.68 ± 2.27
dz$_i$/dSST	(m K^{-1})	17 ± 4
dz$_b$/dSST	(m K^{-1})	32 ± 2
dLHF/dSST	(W m^{-2} K^{-1})	2.89 ± 0.74

the constant and the stochastic forcing experiment. The signs of the regression coefficients for z_i and z_b are consistent with the LES results (Tables 3 and 4). However, a stronger dependence on LTS with respect to Δq_t is found. The pattern of $\langle q_t \rangle$ is consistent with the LES results (Table 5), while $\langle \theta_l \rangle$ shows a partial consistency only for the stochastic forcing experiment (Table 6). Only for that experiment the boundary layer is found to become warmer for a weaker LTS. Finally the patterns of the surface fluxes are not consistent with the LES results (Tables A7 and A8).

The model ensemble mean of the cloud fraction vertical profiles for the cases considered before are displayed in Figure 9. The cloud fraction profile of each model has first been averaged in time over the last 80 days of simulation and successively interpolated on the coarsest resolution grid, i.e., on CNRM grid (solid lines in Figure 9). An estimate of the spread among models is given by the standard deviation (shaded area in Figure 9). The SCM ensemble mean is compared to the LES profiles (red dashed lines). The model ensemble mean profiles are not strongly affected by the additional stochastic noise added to the subsidence. The cloud layer is rather thick compared to the LES profiles and the maximum cloud fraction is much smaller than the LES values. This is also an effect of the interpolation on a coarser vertical grid. In a more qualitative perspective the SCM ensemble mean profiles show a deepening of the boundary layer for cooler and drier free tropospheric conditions, in agreement with the LES results.

4.2.7. Quantitative Comparison With the LES Results

To make a more quantitative comparison between the SCM and the LES results the correlation coefficient, R, is used. This measure quantifies the similarities between two patterns, i.e., the SCM and LES results, for a variable ψ (ψ^s and ψ^l, respectively) and it is defined as

$$R = \frac{\frac{1}{N_i \cdot N_j} \sum_{i=0}^{N_i} \sum_{j=0}^{N_j} (\psi^s{}_{i,j} - \overline{\psi^s})(\psi^l{}_{i,j} - \overline{\psi^l})}{\sigma^s \sigma^l}, \tag{8}$$

where $\overline{\psi}$ indicates the average mean state over the whole phase space and σ is the standard deviation within the phase space. The correlation coefficient varies between 1 and -1 and reaches the maximum value when the two patterns vary consistently in the phase space independently of the quantitative details. Note that if at least one of the two patterns does not vary within the phase space the correlation coefficient cannot be calculated. To evaluate the model systematic errors the mean bias is introduced

$$\mu = \overline{\psi^s} - \overline{\psi^l}. \tag{9}$$

The mean bias is positive when the SCM results are overestimated on average and negative otherwise. Differently to the correlation coefficient this measure is unbounded. To highlight the relative importance of the mean bias with respect to the benchmark, $\overline{\psi^l}$ and σ^l are reported in Table 4 for LWP, z_i, z_b, $\langle q_t \rangle$, $\langle \theta_l \rangle$, LHF, and SHF. Note that R and μ do not give information on the amplitude of the dependence of the considered variables on the
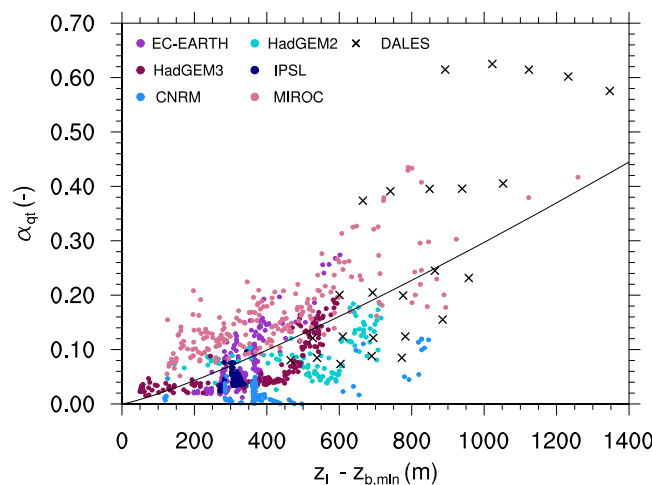

Figure 7. Scatterplot of the decoupling parameter, α_{q_t}, as a function of the cloud layer depth. The line represents the observed relationship [*Park et al.*, 2004]. The SCM results are obtained by adding a stochastic noise to the subsidence.
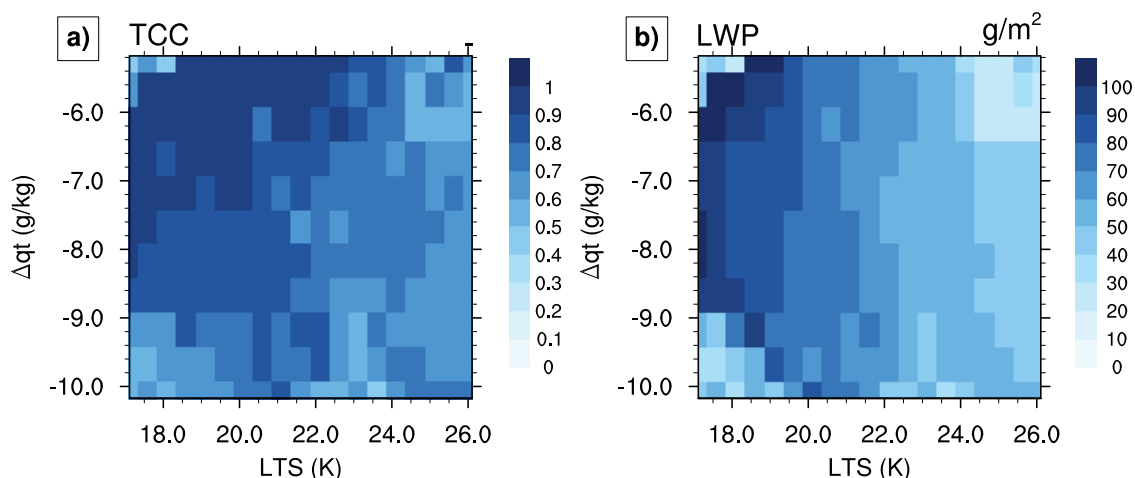
Figure 8. Mean states of TCC and LWP of the SCMs model ensemble mean results of the stochastic forcing experiment.

free tropospheric conditions. To this end we use the linear regression coefficients b_1 and b_2 for the LES and SCM results (Tables (A1–A8)).

Figure 10 shows the performances of each model using the previously introduced measures. The perfect pattern would have no bias and a correlation coefficient equal to one. This reference point is highlighted in the plots by a red dot. This analysis is performed for the previously introduced variables z_i, z_b, $\langle q_t \rangle$, $\langle \theta_l \rangle$, LHF, SHF, and LWP. Moreover, the in-cloud LWP (LWP_c) defined as $LWP_c = LWP/TCC$ and the surface precipitation (P) are considered. The results for the constant forcing and the stochastic forcing experiments are shown. For consistency only the subset of cases for which LESs are available is considered.
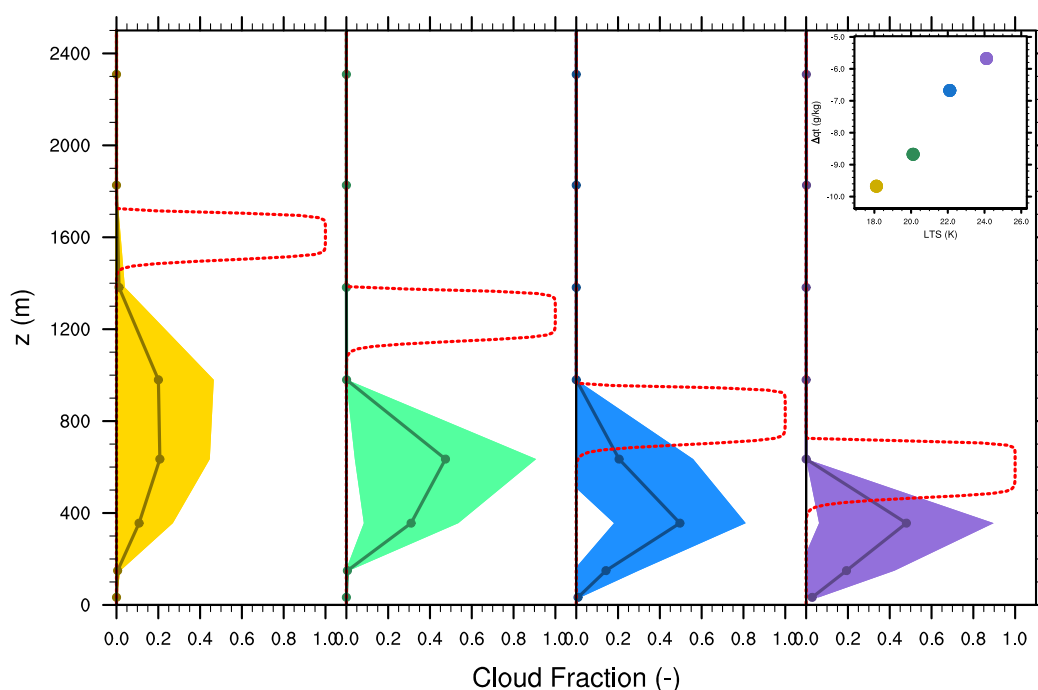

Figure 9. Same as Figure 6, but for the SCM model ensemble mean results of the stochastic forcing experiment. The shaded area represents the variability of the profiles and it is estimated through the standard deviation.
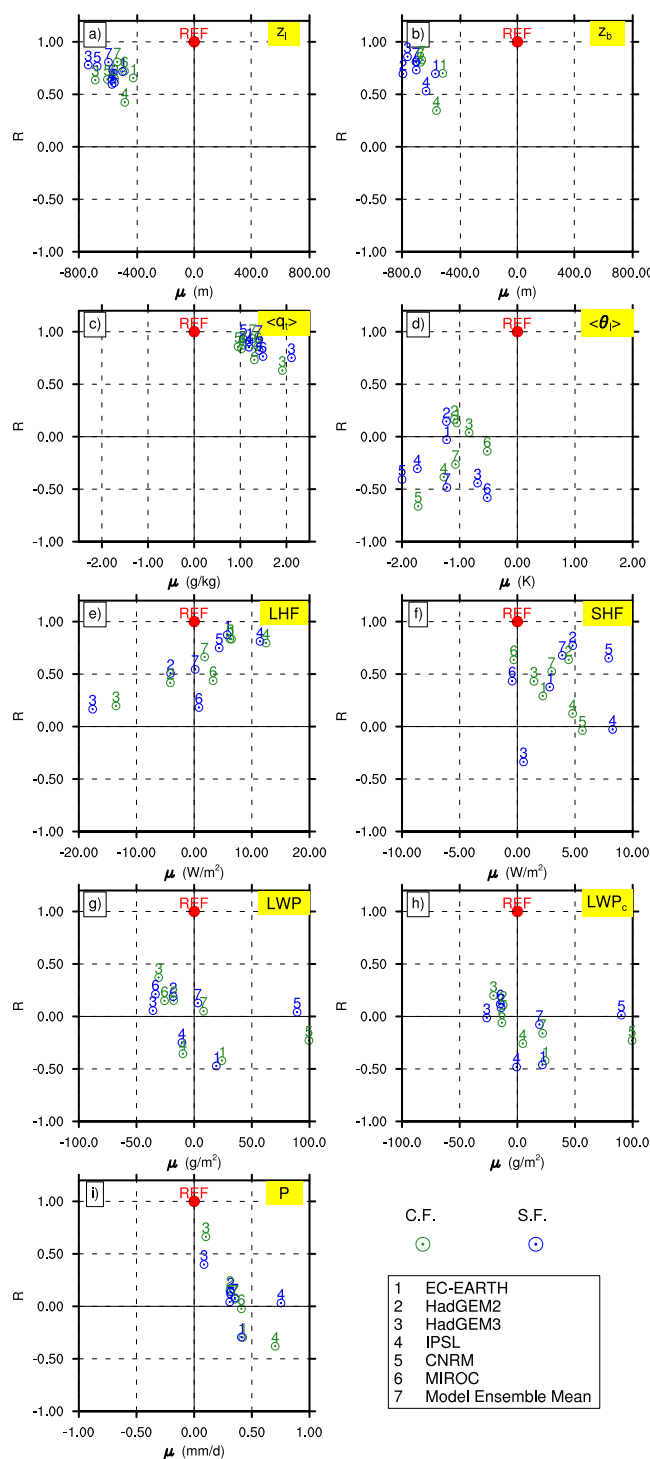
Figure 10. Quantitative comparison between SCM and LES results: the correlation coefficient, R, and the mean bias, μ, are used. The red dot indicates the reference point corresponding to the ideal performance.

It is remarkable how the SCMs show several common behaviors highlighted by the clusters of points in Figure 10. It does not come as a surprise then that the model ensemble mean is affected by the same biases and does not present a better performance than the SCMs. Despite the fact that for z_i an increase in the correlation coefficient is found when a stochastic noise is added to the subsidence, a systematic improvement in the SCM performances for the stochastic forcing experiment is not clearly found from this analysis.

The analysis of the correlation coefficient confirms that the dependence of z_i, z_b, $\langle q_t \rangle$, and LHF on the free tropospheric conditions is well described by the SCMs (Figures 10a, 10b, 10c, and 10e). However, the variation of z_i, z_b, and $\langle q_t \rangle$ is weaker than in the LES results (Tables (3–5)), while $\langle \theta_l \rangle$ presents a too strong dependence on the free tropospheric conditions (Table 6). The pattern of the SHF is not consistent with the LES results, as the values of R are rather low (Figures 10f) and its variation in the phase space is too large (Table A8). The latter can be understood on the basis of the too strong dependence of $\langle \theta_l \rangle$ on the free tropospheric conditions. Furthermore, all the SCMs predict a boundary layer which is too shallow, too moist, and too cool with a consequent systematic underestimation of the cloud base height (Figures 10a–10d). The surface fluxes tend to be systematically overestimated (Figures 10e and 10f). The SHF overestimation is an effect of the too cool boundary layer, while the LHF is directly related to the excess in precipitation (Figures 10i). The underestimated TCC seems to be the reason of a systematic underestimation of LWP (Figure 10g). In fact, when a proxy of the in-cloud liquid water, LWP_c, is considered, the SCMs do not show a common behavior (Figure 10h). Moreover, a too low TCC affects the LW cooling at the cloud top with a consequent decrease in the turbulence at the inversion leading to a too shallow boundary layer.
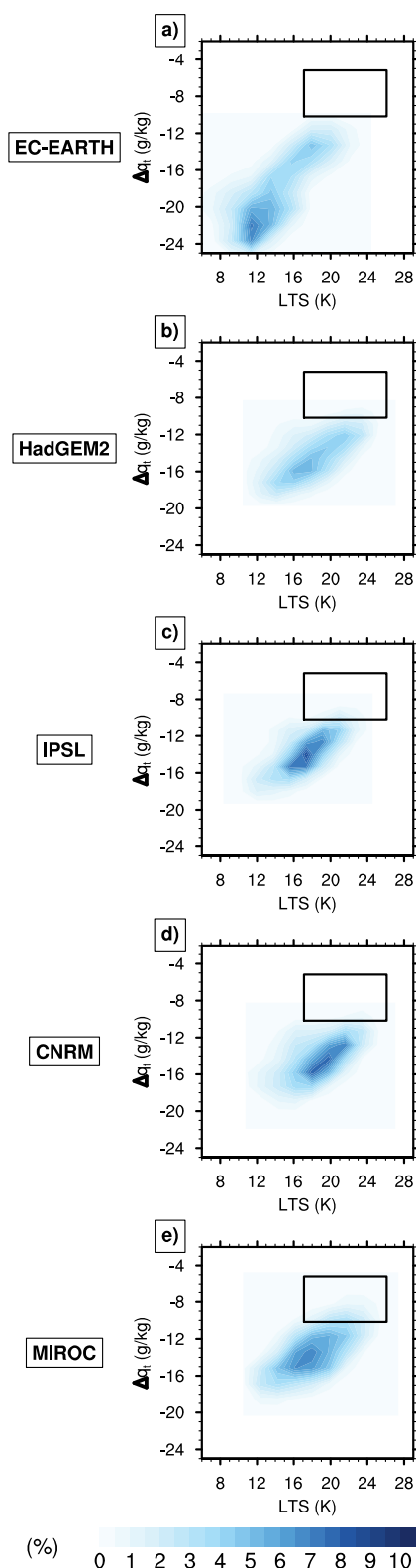
Figure 11. Frequency of occurrence of LTS-Δq_t combinations. The joint probability density function is calculated for five host GCMs participating to CMIP5 project, run in the atmospheric-only mode (AMIP). The analysis is performed for the Scu regions defined in Table 3. The black box indicates the region of the phase space investigated by the SCMs and the LES.

The biases previously summarized are long-standing problems which also affect the GCM results [*Lin et al.*, 2014]. *Duynkerke et al.* [2004] drew the same conclusions by comparing SCM results to both observations and LESs. In that article an explicit parameterization of the entrainment flux at the cloud top was recommended. In this study three models (EC-EARTH, HadGEM2, and HadGEM3) have such a parameterization (Table 2) but still do not show a particularly good performance. *Boutle and Abel* [2012] suggested that a more accurate representation of the microphysical processes is necessary to obtain a more realistic representation of the Scu-topped boundary layer. From this analysis it is not possible to identify which is the process that, through its representation, contributes the most to the previously discussed biases. However, it is clear that further work is needed to improve the current representation of Scu clouds in GCMs.

4.3. On the Correspondence to the Host GCMs

The following analysis is meant to assess the correspondence between the previous results and the outputs of the host GCMs. The results of EC-EARTH, HadGEM2, IPSL, CNRM, and MIROC of the AMIP experiment, belonging to the CMIP project, are used; hence, the outputs of the models in their atmosphere-only modes are considered. Only the Scu regions defined in Table 3 are taken into account. The different atmospheric regimes are determined on the basis of LTS and Δq_t alone; hence, no additional conditional sampling is applied. The underlying hypothesis is that the most important cloud-controlling factors for Scu are LTS and Δq_t and they alone determine the cloud regime.

To identify the conditions with the highest frequency of occurrence, Figure 11 shows the joint probability density function (PDF) of the LTS-Δq_t combinations. It is noticeable that all models present a correlation between the two bulk jumps. More precisely, a weaker Δq_t corresponds, most likely, to a larger LTS, and vice versa. These bulk jumps are mainly controlled by the SST, as the free tropospheric conditions tend to vary less than the surface conditions. A higher SST tends to result in a weaker LTS and a stronger Δq_t, and vice versa for a lower SST.
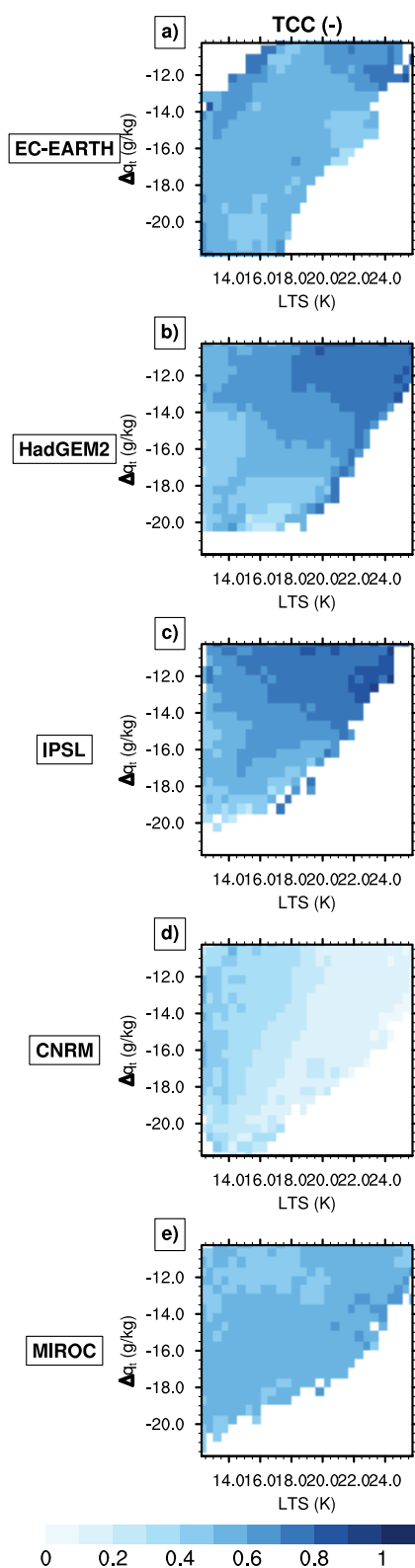
Figure 12. Mean state of the TCC of all the host GCMs. The results are obtained by binning the GCM outputs according to the LTS-Δq_t combinations. The analysis is performed for the Scu regions defined in Table 3. The white regions in the phase space correspond to the atmospheric conditions for which no results are found.

We define the region of interest for the following analysis as:

$$LTS = [12; 26]K;$$

$$\Delta q_t = [-22; -10] \text{g kg}^{-1}.$$

This region does not coincide with the one considered in the SCM experimental setup (black box in Figure 11). In particular, the two ranges of Δq_t do not correspond, whereas the LTS range analyzed by the experimental design is included in the range used for GCM outputs. The reason for this discrepancy is twofold. First, the assumption of constant q_t with height considered in the SCM experimental design leads to lower values of Δq_t for the same conditions at the inversion. Second, the average SST over the whole data set is 299 K, i.e., 7 K higher than the one provided by the SCM experimental setup. As already discussed, a warmer sea surface promotes a higher LTS and a stronger Δq_t. Consistent with CGILS project, our SCM experiment has been set up on the basis of observations at the location S11 (32°N–129°W), along the GPCI (GEWEX Pacific Cross-section Intercomparison, where GEWEX stands for Global Energy and Water cycle EXchanges Project) transect in the Northeast Pacific [*Siebesma et al.*, 2004; *Teixeira et al.*, 2011]. This is on the Northern border of the Californian region, which is the one located furthest from the Equator among the Scu regions (Table 3). For this reason, the SST prescribed in the SCM experimental design is lower than the average value calculated for the AMIP experiment.

The mean states of TCC and LWP are displayed in Figures 12 and 13, respectively. The results are obtained by binning the GCM outputs according to the LTS-Δq_t combinations, where the bins are 0.5 K and 0.5 g kg^{-1} wide. The patterns differ from model to model. EC-EARTH and MIROC do not show large variations of TCC in the phase space (Figures 12a and 12e). HadGEM2 and IPSL present a decreasing TCC and LWP toward weaker LTSs and stronger Δq_t (Figures 12b, 12c, 13b, and 13c). Finally, for CNRM TCC and LWP have higher values for increasing
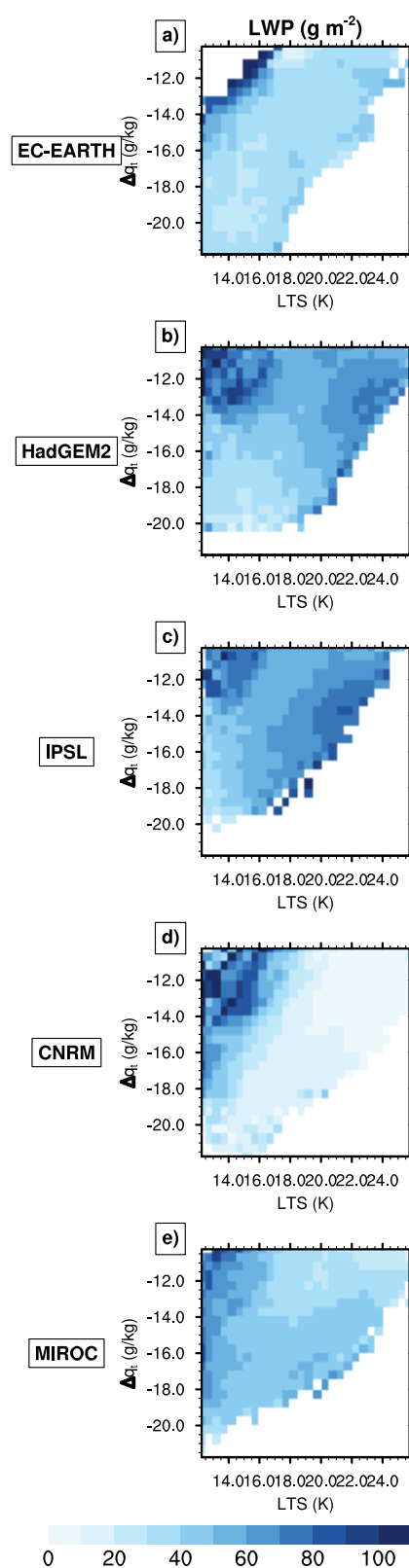
Figure 13. Same as Figure 12, but for LWP.

LTSs and Δq_t (Figures 12d and 13d), i.e., opposite with respect to HadGEM2 and IPSL. For none of the models is a clear correspondence between Figures 12 and 13 and Figures 4 and 5 found. This might be due to a too idealized experimental design. A complete discussion of the possible improvements that can be applied to the setup is reported in section 5.4.

To assess the variability of the mean states, the standard deviation is calculated for each bin and then averaged over the whole phase space. The values are reported in Table 5 for both TCC and LWP. In general, the standard deviations are relatively high as compared to the mean values presented in Figures 12 and 13, and hence the variability within each bin is large. This suggests that other cloud-controlling factors might play an important role in determining the Scu regime. Considering only LTS and Δq_t is a simplification in itself and its effect on these results should be further investigated.

5. Response to a Climate Perturbation

5.1. LES Results

The response of a variable ψ to a climate perturbation is estimated as the difference between the perturbed climate experiment results and the control climate experiment results normalized by the SST increase, $d\psi/dSST$. In particular, the response of the total cloud radiative effect (CRE) will be considered as an estimate of the cloud feedback. The cloud radiative effect is defined as the difference between the net downward radiative flux at the top of atmosphere in total sky and in clear-sky conditions [*Cess et al.*, 1989]. The CRE response has been widely used in literature to quantify the cloud response to a climate perturbation [e.g., *Zhang et al.*, 2013]. In the upcoming sections it will be considered as a proxy for the cloud feedback, such that a positive value of dCRE/dSST will be interpreted as a positive cloud feedback and a negative value as a negative cloud feedback.

Figure 14 shows the CRE response obtained with DALES. The cloud feedback is positive in the whole phase space. Since no Scu breakup is found, the cloud response is due to a LWP change only. More precisely, the LWP decreases as a consequence of a boundary layer drying. In a warmer climate, DALES predicts an increase in both the LHF and in the humidity flux at the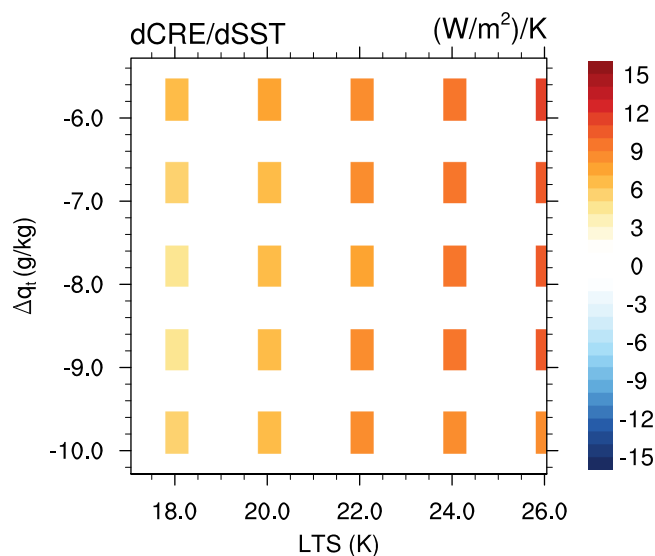 cloud top due to entrainment. The former has a moistening effect and the latter a drying effect, as it implies the mixing of relatively dry air from the free troposphere. The entrainment is enhanced by the increase in the LHF and suppressed by the

Figure 14. DALES results of the mean state of the response of CRE to the prescribed climate perturbation (dCRE/dSST).

decrease in the radiative flux divergence, due to the humidification of the free troposphere [*Dal Gesso et al.*, 2014a]. The response in the radiative flux divergence at the cloud top found in the LES results is modest, of the order of 0.5 W m^{-2}. As a result, the dominating effect is the increase in LHF which leads to a deeper boundary layer. Consequently, the LES results exhibit an overall decrease in the RH, which causes the cloud base to rise. The change in the cloud base height is found to be larger than the one in the cloud top height with a consequent cloud thinning. The strongest response is found for stronger LTSs, for which the boundary layer is shallower and more well mixed. The LWP variations are consistent with the LES results of the CGILS project, for the experiments corresponding to well-mixed (S12) and decoupled Scu (S11), with a similar climate perturbation [*Blossey et al.*, 2013; *Bretherton et al.*, 2013].

5.2. SCM Results
5.2.1. Cloud Response
The same analysis is performed for the SCM results and the CRE response obtained by each model is displayed in Figure 15. For the sake of completeness we include also the results of the constant forcing experiment. However, as for the control climate experiment, the model fingerprint in the phase space is similar for the two experiments.

The main difference between the LES and the SCM results is that the latter do not show a consistent pattern in the phase space. For small changes in the free tropospheric conditions, large changes in both the sign and the magnitude of the CRE response can be found. This results in a rather noisy pattern that does not show any clear dependence on LTS and Δq_t.

Differently to DALES, the cloud feedback found with SCMs is due to changes in both the TCC and the LWP. EC-EARTH (Figures 15a and 15b), IPSL (Figures 15g and 15h), and MIROC (Figures 15m and 15n) do not present strong variations in the TCC. More precisely EC-EARTH shows a TCC decrease in the lower left corner of the phase space only for the stochastic forcing experiment. A similar response is found for CNRM (Figures 15i and 15l) for both the constant and stochastic forcing experiment. Moreover, in the upper right corner of the phase space a band with a net TCC increase is found. These cases correspond to a clear-sky regime in the control climate experiment but show a totally overcast boundary layer in the perturbed climate experiment. In the regions of the phase space where the TCC does not change the CRE response only depends on the change in the LWP. EC-EARTH presents a net LWP increase, while both IPSL and CNRM predict a LWP decrease consistent with the LES results. For MIROC, a rather scattered pattern is found for both TCC and LWP, as in Figures 15m and 15n. HadGEM2 exhibits a strong TCC decrease in a large area of the phase space corresponding to drier free tropospheric conditions. For HadGEM3 a strong TCC decrease is found for moister and warmer free tropospheric conditions (upper right corner of the phase space). At the edge of the region corresponding to clear-sky conditions in the control climate experiment, a band of Scu-topped boundary layer cases is found in the perturbed climate experiment, causing a strong CRE decrease.

Only two of the considered models participated in the CGILS model intercomparison study [*Zhang et al.*, 2013], namely HadGEM2 and IPSL. The present study applies an experimental design which is a
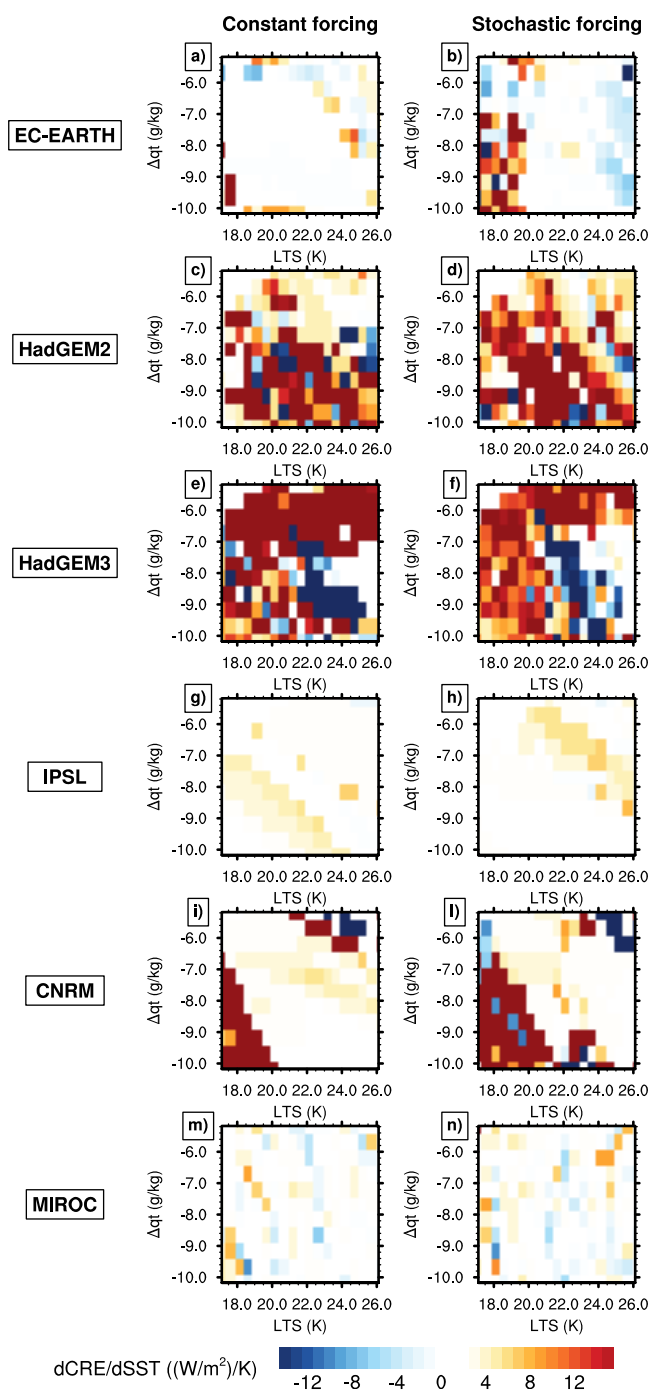
Figure 15. Mean state of the dCRE/dSST of all the considered SCMs. The results of the (left) constant forcing experiment and (right) stochastic forcing experiment.

simplified version of the CGILS setup. In the CGILS project, horizontal advection of humidity and temperature are considered. Other details, such as the wind velocity and the subsidence, are more realistic than in the present study being based on observations. Furthermore, in CGILS the climate perturbation includes a subsidence reduction, aimed to mimic the weakening of the Hadley circulation, which is ignored in the present study. However, in *Zhang et al.* [2013] the predicted cloud feedback for experiment S12 (well-mixed Scu) and S11 (decoupled Scu) by HadGEM2 and IPSL is positive and a stronger response is given by HadGEM2. Therefore, the general CRE response found in this study is in agreement with the CGILS results for HadGEM2 and IPSL.

Figure 16 displays the model ensemble mean results of dCRE/dSST. Even for the model ensemble mean, abrupt changes in both the magnitude and the sign of the cloud feedback are found for small changes in the free tropospheric conditions. However, the cloud feedback is mainly positive with a stronger contribution coming from the region with lower LTS values and stronger Δq_t. This is actually opposite of what is found in the LES results where the stronger response corresponds to greater LTSs.

To summarize the results, Table 6 collects the average and the standard deviation over the whole phase space of dCRE/dSST for all the SCMs. The values can be compared to the LES result reported in Table 7. All the SCMs predict an overall positive feedback consistent with the LES results. The spread among models is rather large and comparable to the one found in the CGILS experiments corresponding to well-mixed (S12) and decoupled Scu (S11), for the models giving the same sign of the feedback.

5.2.2. Quantitative Comparison With the LES Results
To more quantitatively compare the response of z_i, z_b, LHF, CRE, and LWP predicted by the SCMs with the LES results, the correlation coefficient and the mean bias are considered. The results of this analysis are
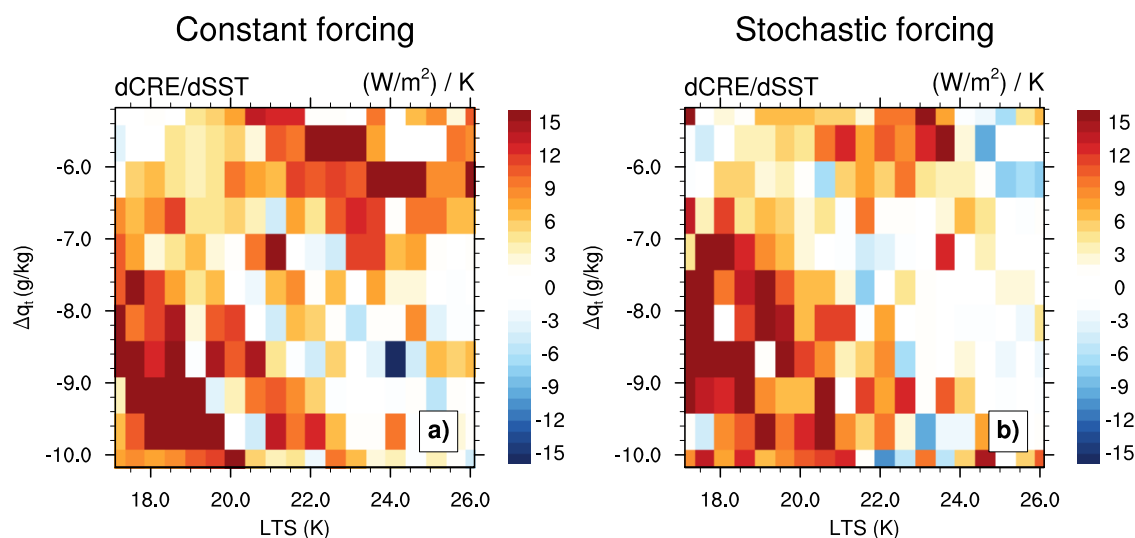
Figure 16. Same as Figure 15, but for the SCM model ensemble mean results.

displayed in Figure 17 and the average values over the phase space of the LES results are collected in Table 7. In this case we distinguish between the models that do not capture the sign of the response for a particular variable and the models that do agree with the LES results. Moreover, the mean bias is divided by the sign of the LES response. In this way the response of the SCMs is underestimated if μ is negative and overestimated otherwise, independently of the sign of the LES response. Note that the largest biases are due to a disagreement on the sign of the feedback.

Apart from some exceptions, the correlation is rather low for all the SCM responses. The beneficial effect of the introduction of a stochastic component into the subsidence is evident from the results of this analysis, as several SCMs predict a boundary layer deepening only for the stochastic forcing experiment. It is worth stressing that the biases for $dz_i/dSST$ (Figure 17a) and $dz_b/dSST$ (Figure 17b) are comparable to the LES responses (see Table 7), though changes of the order of tens of meters (i.e., smaller than the grid size) as found in the LES results, are difficult to be predicted with a SCM. Consistent with the CGILS results [*Zhang et al.*, 2013] and GCM studies [e.g., *Webb et al.*, 2001], all the SCMs predict an increase in LHF (Figure 17c). An exception is HadGEM2 for the stochastic forcing experiment. In this case the particular selection of cases includes several cases corresponding to clear-sky conditions in the perturbed climate leading to a strong LHF decrease which dominates in the average value. However, in the majority of the phase space this model presents a LHF increase for both the constant and stochastic forcing experiments (not shown). Similar considerations are valid for EC-EARTH and MIROC in the case of the responses of CRE and LWP (Figures 17d and 17e). The other SCMs agree in sign with DALES but tend to underestimate the cloud feedback. In fact, in the area of the phase space where the TCC does not strongly change with respect to the control climate experiment, which is generally large, $dLWP/dSST$ is rather small.

In conclusion, there is a consistency in sign between the cloud feedback estimated with the LES and the SCMs. However, it is not clear whether that would still be the case if the SCMs did not predict a decrease in the TCC. The results summarized in Table 6 suggest that without a TCC change the cloud feedback is of the order of 1 $Wm^{-2}K^{-1}$ or even less (see EC-EARTH, IPSL, and MIROC).

5.3. Scu Response in the Host GCMs
It is worth comparing these results with the Scu responses obtained by analyzing GCM outputs. To this end, the normalized CRE responses as a function of LTS and Δq_t are shown in Figure 18. The results are calculated for the outputs of the host GCMs, run in their atmosphere-only mode for present-day climate SSTs (AMIP experiment) and for a uniform increase of 4 K (AMIP4K experiment).
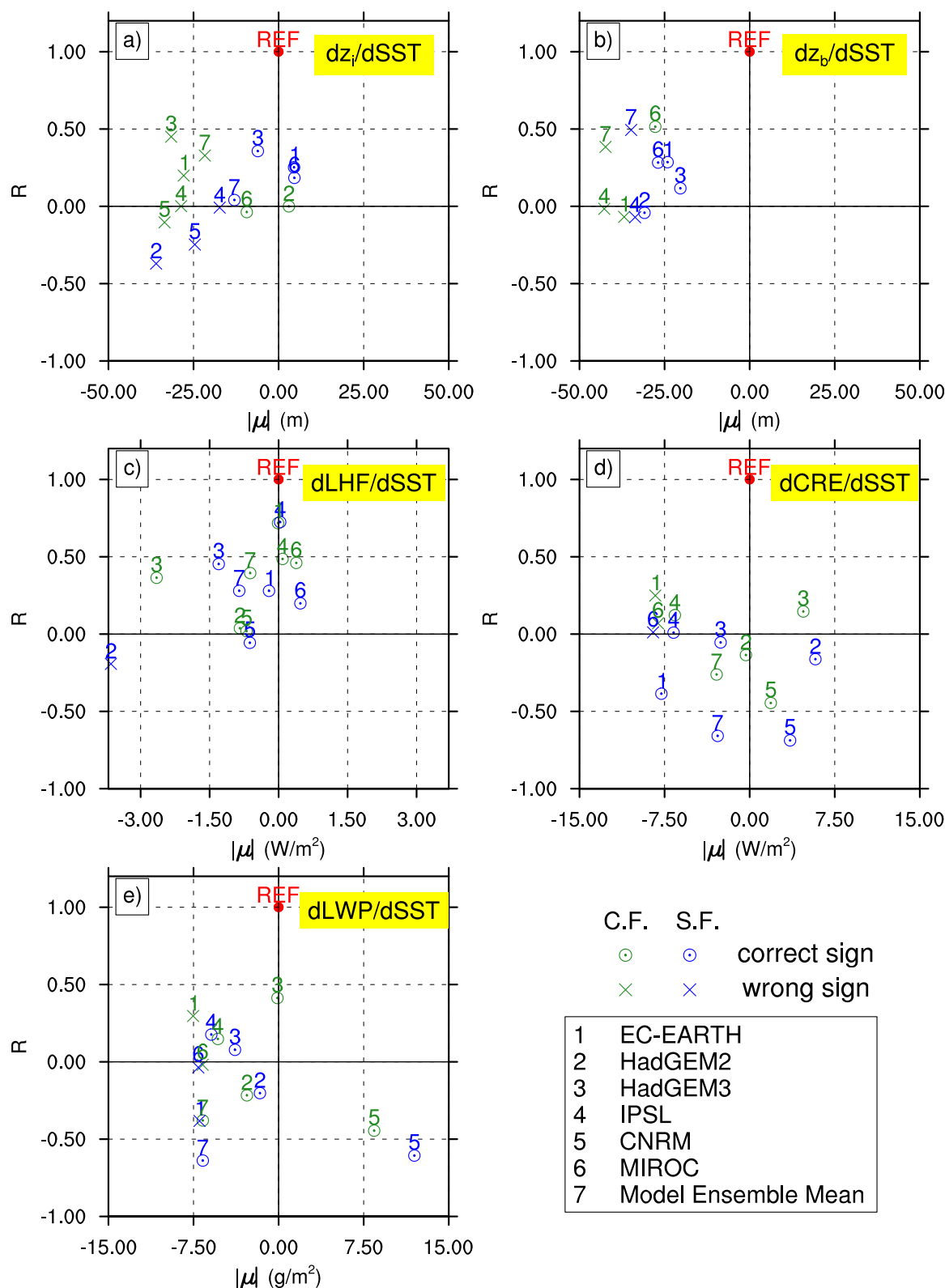
Figure 17. Same as Figure 10, but for the response to a perturbed climate.

Different from the SCM and LES results, CRE is labeled for both AMIP and AMIP4K experiments by the actual LTS and Δq_t values. All the models present a rather homogeneous pattern in the phase space, with no clear dependence on the bulk jumps. All the host GCMs forecast positive values for the CRE

response in a major part of the phase space. An exception is CNRM which shows negligibly small variations of CRE in the whole phase space.

The total Scu response is calculated by weighing each bin by the relative frequency of occurrence as

$$\left.\frac{d\text{CRE}}{d\text{SST}}\right|_{\text{tot}} = \frac{1}{d\text{SST}} \sum_{i=0}^{N_i} \sum_{j=0}^{N_j} \left[\left(\text{CRE}_{i,j}^{\text{PC}} \wp_{i,j}^{\text{PC}} \right) - \left(\text{CRE}_{i,j}^{\text{CTL}} \wp_{i,j}^{\text{CTL}} \right) \right],$$ (10)

where $\wp$ is the joint PDF for each combination of LTS-Δq_t, identified by the indexes i and j. Note that the joint PDF is normalized, so its integrated value in the whole phase space is 1. A similar approach is applied to SCM and LES results. As there is no overlap between the considered regions of the phase space, we cannot use the joint PDF calculated on the basis of the GCMs output. We assume that all cases entailed by the experimental design have the same frequency of occurrence, i.e., $1/(N_i \cdot N_j)$.

Figure 19 shows on the x axis the SCM results of $d\text{CRE}/d\text{SST}|_{\text{tot}}$ and on the y axis the values calculated from GCM outputs. If a correspondence in both sign and magnitude was found, all the markers would be on the diagonal. For all the models the sign of the feedback is consistent between SCM and GCM results, but only for HadGEM2 we find a correspondence also in magnitude. Except for CNRM, the Scu response found with SCMs is underestimated with respect to the one obtained with the host GCMs. Finally, Figure 19 includes also the total CRE response calculated from LES results (red marker). The overall Scu response estimated by DALES is comparable to the ones obtained from GCM outputs. However, GCMs predict both a decrease in TCC and LWP (not shown), while the LES results present the same overall change in CRE but due only to a variation in LWP. This suggests that the Scu feedback forecast by GCMs might be underestimated, because the component due to the change in LWP alone is not predicted.

It is also worth stressing that the climate perturbation considered in the SCM experimental design is a simplification of the local changes taking place in the Scu regions. In GCMs, the climate warming results in both the increase in the SST (which in the case of AMIP4K is imposed) and in circulation changes as well as in other feedbacks. The comparison between SCM and GCM results gives hints on the contribution due to the circulation changes or other factors. When the SCM and GCM results coincide, as for HadGEM2, the major contribution to Scu response comes from the sea surface warming. Changes to the global circulation and other feedbacks do not significantly affect the Scu. When the response in the SCM is stronger than in the GCM, as for CNRM, circulation changes and other factors are likely to offset the effects of the SST variation. On the contrary, when the stronger response is found for GCM results (EC-EARTH, IPSL, and MIROC), the response to a SST increase is relatively small as compared to the one due to other factors. This suggests that the Scu response in these GCMs is mainly controlled by circulation changes. To conclude, the uncertainty on Scu feedback is equally due to the differences in the response of the GCMs to a SST increase and the contribution of circulation changes and other factors. These hypotheses on the major contributor to the Scu feedback in the GCMs considered should be further explored in future studies.

5.4. Discussion

The present paper is part of a large scientific effort evaluating the representation of the low-cloud feedback in climate models. Aimed to be an extension of CGILS, the present setup has been used in several studies performed with different models, including a MLM, a LES, and several SCMs. The advantages of this setup are numerous. First, the SCM and the LES results can be compared to the CGILS results and can be used to extend that project. Second, considering a wide range of cases is necessary because of the abrupt changes in both the sign and the magnitude of the Scu response for small changes in the free tropospheric conditions, found for all the SCMs. Lastly, the setup is rather idealized and hence the outcome is relatively easy to interpret. This is advantageous considering how delicate the interaction between all the different physical mechanisms and the corresponding parameterizations in the Scu-topped boundary layer is.

Nevertheless, the lack of correspondence with the results of the GCMs suggests that the experimental design might be too idealized to represent the model behaviors in the Scu regions. Considering equilibrium states is not a realistic choice. Moreover, with the vertical resolution used in SCMs, the achievement of an equilibrium might not be trivial and might be affected by numerical artifacts
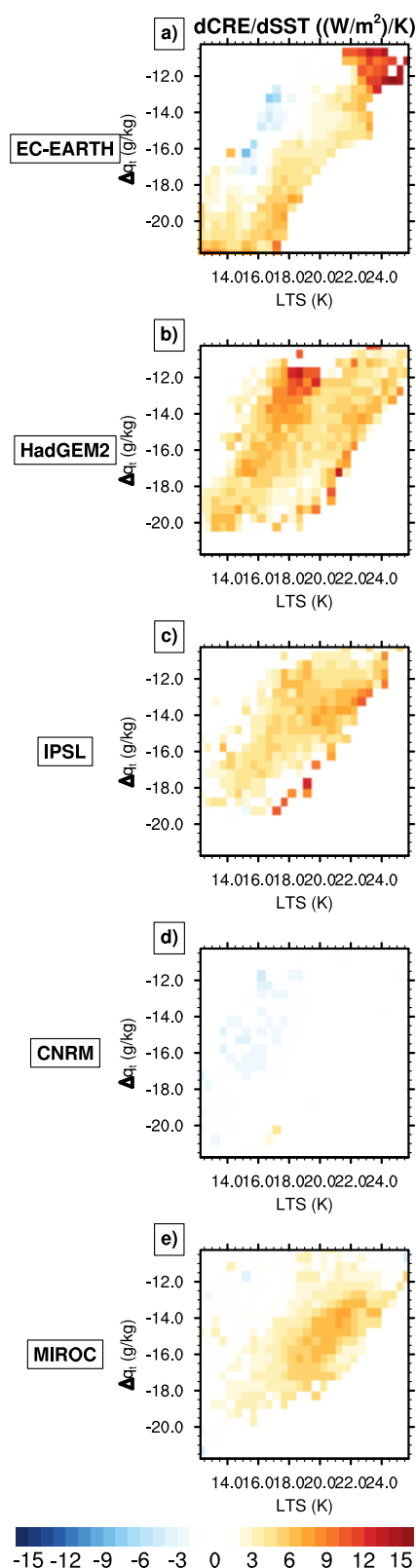
Figure 18. Mean state of the dCRE/dSST of all the host GCMs. The control climate results are obtained from AMIP experiment and the perturbed-climate results from AMIP4K experiment.

[e.g., *Lenderink and Holtslag*, 2000]. In this respect, the use of an additional stochastic noise that is added to the subsidence is beneficial, as highlighted especially in the perturbed climate experiments. However, the stochastic noise should be further increased by using a wider range of stochastic numbers (defined by δ_w, equation (3)). In this way, a larger variability of the subsidence is considered and the models would respond more clearly to these variations. At the same time, stronger variations of the subsidence might trigger the disappearance of Scu clouds (as described for HadGEM3). The reformation of clouds can be aided by the presence of the horizontal advection of cold air, which is a typical feature of the Scu regions. Including the horizontal advection of cold air leads also to an increase of SHF at the surface. The present experimental setup is characterized by weak surface fluxes, as clarified by the LES results. In the case of the SHF, this is indeed due to the lack of horizontal temperature advection, but it is also enhanced by the presence of Scu, which leads to a weak radiative cooling below the cloud layer. Concerning LHF, the increase of the prescribed SST results in an enhancement of the humidity flux at the surface, for a fixed RH. A higher SST would also lead to a stronger Δq_t, for the same free tropospheric conditions. In that case, the area of the phase space mapped by the experimental design would be in line with the region where the PDF calculated from GCM outputs is located. By applying all these improvements to the setup, a more direct comparison to GCM results would be possible. However, similar changes should be also applied to the prescriptions used for LES models, to maintain the results consistent with SCM outputs. In particular, the stochastic component of the subsidence should also be considered for LES models.

Independently of the correspondence with the host GCMs, the comparison with LES results suggests that the description of the Scu-topped boundary layer in SCMs is still inadequate. This might be affected by the selected benchmark, though this cannot be tested. Since this setup is so idealized and includes an experiment aimed to mimic perturbed climate conditions, the LES results cannot be directly compared to
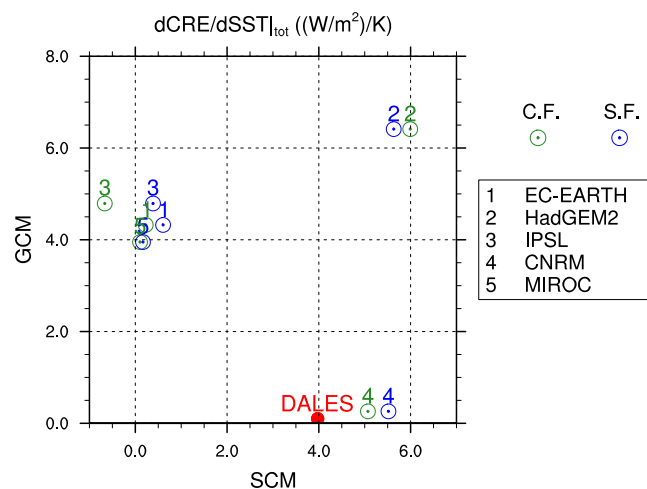
Figure 19. Correspondence between the total Scu response (dCRE/dSST$|_{tot}$) calculated by the SCMs (on the *x* axis) and the host GCMs (on the *y* axis). The red marker corresponds to the value estimated from the LES results. This marker is located on the *x* axis because the LES results can be compared only to the SCM results. The total CRE response is calculated by integrating over the whole phase space dCRE/dSST. In the case of GCM outputs the joint probability density function of the LTS-Δq_t combinations is used to weigh each bin by the frequency of occurrence.

observations. Moreover, currently DALES is the only LES model participating in the present intercomparison study; thus, its results cannot be corroborated by the comparison with other LES models. On the other hand, *Blossey et al.* [2013] found that for both decoupled (experiment S11) and well-mixed (experiment S12) Scu-topped boundary layer the response of LES models was consistent if the reduction of the subsidence was neglected. This gives us confidence in the reliability of the LES results. The only weakness worth stressing is the selected vertical grid (vertical resolution of 10 m), chosen for limiting the computational cost. Sensitivity studies demonstrate that with a vertical resolution of 5 m the boundary layer is less decoupled and presents a thicker cloud layer, hence higher LWP values. Except for this difference, the results with a higher vertical resolution are qualitatively comparable to those obtained with a coarser vertical grid. These considerations do not affect the evaluation of the Scu representation in SCMs, as the majority of the SCMs underestimate the LWP and this bias would become even more noticeable if a higher vertical resolution was considered for DALES. Besides, the biases that affect the SCMs, highlighted in the control climate experiment analysis, are well-known deficiencies of the 3-D and SCM versions of GCMs [e.g., *Siebesma et al.*, 2004].

Lastly, it is interesting to discuss the effects of the vertical resolution on the SCM's spread and on their common biases. As a preliminary sensitivity study, we can compare EC-EARTH results with the results presented in *Dal Gesso et al.* [2014b]. The same experimental design is employed to investigate in detail the representation of Scu clouds in EC-EARTH SCM with a higher vertical resolution grid (80 levels in total and 17 levels in the first kilometer of atmosphere) as compared to the operational version (Table 1). Substantial improvements in the results are not found, as the LWP is still underestimated and the boundary layer is still too shallow, too moist, and too cool as compared to DALES results. It is actually found that EC-EARTH with a higher vertical resolution predicts a TCC reduction for weak LTSs; hence, a stronger bias with respect to DALES results as compared to the results presented here. Another difference is that the stochastic noise added to the subsidence is clearly beneficial in reducing the dependence on the vertical resolution and the initial conditions. As a result, the patterns of TCC and LWP in the phase space show noticeable differences between the results of the constant forcing and the stochastic forcing experiment. Furthermore, the CRE response to the climate perturbation is more distinctly positive with an average value within the phase space of 3.06 W m^2 K^{-1} for the constant forcing experiment and of 4.08 W m^2 K^{-1} for the stochastic forcing experiment. These results suggest that the vertical resolution has indeed an impact on the Scu response to a climate perturbation. However, if the physical parameterizations are not adequate, an increase in the vertical resolution does not necessary improve the model representation of the Scu-topped boundary layer.

6. Summary and Conclusions

The present article considers a hierarchy of models to assess the dependence of Scu clouds on the thermodynamic conditions in the free troposphere, identified by LTS and a similar measure for humidity, Δq_t. A LES model is used as a benchmark for evaluating six SCMs. The results of the SCMs

are then compared to the outputs of the host GCMs to clarify the correspondence to the 3-D counterpart. For SCMs and LES, two sets of large-scale forcing conditions are considered: one for the present-day climate and one for a future climate scenario. The imposed climate perturbation includes an increase in the SST and a consequent warming and moistening of the atmosphere, as an effect of the unperturbed RH. The GCM outputs are obtained by running the models in their atmosphere-only mode. Two sets of prescribed SSTs are used, one including observed values and the second one the same values increased by 4 K (AMIP and AMIP4K, respectively). Only the subtropical regions dominated by Scu clouds are considered.

In the control climate experiment, all the SCMs present similar overall biases. The Scu-topped boundary layer is too shallow, too moist, and too cool. Furthermore, the representation of this regime suffers from an underestimation of the TCC and the LWP and an overestimation of the precipitation. These are long-standing issues that have been reported in previous articles on both SCMs and GCMs studies [e.g., *Duynkerke et al.*, 2004; *Siebesma et al.*, 2004]. A common representation of the Scu dependence on the free tropospheric conditions is not found, as the SCMs present a variety of patterns in the phase space defined by LTS and Δq_t. In particular, TCC and LWP show large differences from model to model, from both a qualitative and quantitative perspective and none of the SCMs captures the dependence found in the LES results. More precisely, none of the models shows a constant TCC = 1 in the phase space and a main dependence of the LWP on Δq_t, with a net cloud thinning for drier free tropospheric conditions.

Both the LES and the SCMs predict an overall positive feedback, corroborating the results of *Blossey et al.* [2013]. However, while in the LES results the positive feedback is due to a LWP decrease only, in the SCM results a change in both the TCC and the LWP is found. In particular, only the models that predict a TCC decrease present a cloud feedback which has a magnitude comparable with the LES results. Furthermore, the SCM results show rather noisy patterns in the phase space and a clear dependence on LTS and Δq_t is not found for any of the models. Within the phase space the SCMs exhibit abrupt changes in both the sign and the magnitude of the feedback for small changes in the free tropospheric conditions. Lastly, the patterns of dCRE/dSST differ tremendously from model to model clarifying that the huge spread found in *Zhang et al.* [2013] is not only the effect of considering only a few cases.

The present study highlights that the Scu representation in SCMs is still inadequate and should be improved. To this end, the reasons at the basis of the inability of SCMs to describe the Scu-topped boundary layer need to be further investigated. An accurate analysis of the numerical methods involved in the parameterizations is beyond the interests of the present work but it is for sure an important component. Our analysis is mainly focused on the physical component of the SCMs. The parameterization that contributes the most to the model uncertainties has not been identified. Based on previous studies, we suggest that the lack of a robust and accurate representation of the entrainment at the cloud top as well as the poor representation of the cloud fraction might have a key role. Finally, independently of the physical parameterizations the vertical resolution is not sufficient to resolve the small variation in the cloud thickness resulting in a LWP decrease found in the LES results.

The comparison with GCM results demonstrates that this study proposes a promising approach to bridge between process-oriented studies and global analyses. The sign of the Scu response found in GCMs is captured by all the SCMs. The difference in the magnitudes of the feedbacks between the SCM and GCM results might be due to two causes. First, the lack of a clear correspondence between SCM and GCM results on the dependence of the Scu regime on the free tropospheric conditions suggests that the experimental design might be too idealized. Simple modifications can be applied to improve the applicability of the setup. Increasing the SST, including horizontal advection of cold air and considering a stronger stochastic noise added to the subsidence are highly recommended changes to make the experimental design more realistic and easier to be employed with SCMs. Second, the climate perturbation considered does not include several changes due to the climate warming. The contribution of the neglected variations can be hypothesized on the basis of the comparison of the total Scu response found with SCMs and GCMs. Future research will further investigate the role of the different cloud-controlling factors in determining the Scu feedback in GCMs.

Appendix A

Tables A1–A8, reported below, collect the results of the multiple linear regression analysis presented and discussed in section 4.

Table A1. Regression Coefficients of the Multiple Linear Regression Applied to the TCC Patterns of DALES and All the Participating SCMs[a]

Model	b_1 (% K^{-1})	b_2 (%(g kg^{-1})$^{-1}$)	B_1	B_2	ε (%)
DALES	−0.00	0.00			
Constant Forcing					
EC-EARTH	0.86	0.94	0.27	0.17	8.43
HadGEM2	1.74	5.45	0.22	0.40	20.36
HadGEM3	−5.48	9.75	−0.40	0.42	32.89
IPSL	−0.17	0.40	−0.12	0.17	3.97
CNRM	0.24	−4.72	0.03	−0.30	24.62
MIROC	−6.71	2.51	−0.91	0.20	8.64
M.E.M.	**−1.35**	**1.96**	**−0.35**	**0.29**	**9.86**
Stochastic Forcing					
EC-EARTH	1.17	0.36	0.30	0.05	10.52
HadGEM2	2.26	8.86	0.24	0.55	22.07
HadGEM3	−10.35	6.52	−0.77	0.29	24.46
IPSL	0.20	0.95	0.12	0.34	4.29
CNRM	−0.48	−2.18	−0.05	−0.13	27.78
MIROC	0.05	0.44	0.16	0.89	0.42
M.E.M.	**−0.60**	**1.45**	**−0.13**	**0.18**	**12.78**

[a]Note that M.E.M. stands for model ensemble mean.

Table A2. Same as Table 1 Except for the LWP Patterns

Model	b_1 (g m^{-2} K^{-1})	b_2 (g m^{-2}(g kg^{-1})$^{-1}$)	B_1	B_2	ε (g m^{-2})
DALES	0.02	8.23	0.00	1.12	2.74
Constant Forcing					
EC-EARTH	−3.94	−6.01	−0.51	−0.46	16.29
HadGEM2	−1.73	2.73	−0.26	0.24	17.89
HadGEM3	−5.45	7.35	−0.66	0.53	14.95
IPSL	−1.29	−1.17	−0.81	−0.43	1.71
CNRM	−7.63	−4.38	−0.38	−0.13	51.87
MIROC	−2.37	0.96	−0.91	0.22	2.98
M.E.M.	**−3.93**	**0.24**	**−0.61**	**0.02**	**14.46**
Stochastic Forcing					
EC-EARTH	−3.45	−5.63	−0.50	−0.48	14.33
HadGEM2	−1.49	3.55	−0.25	0.34	15.88
HadGEM3	−6.75	2.34	−0.87	0.18	11.99
IPSL	−0.93	−0.71	−0.81	−0.36	1.52
CNRM	−9.38	−1.10	−0.43	−0.03	55.44
MIROC	−2.82	3.09	−0.91	0.59	4.62
M.E.M.	**−4.57**	**0.75**	**−0.59**	**0.06**	**17.81**

Table A3. Same as Table 1 Except for the z_i Patterns

Model	b_1 (m K^{-1})	b_2 (m(g kg^{-1})$^{-1}$)	B_1	B_2	ε (m)
DALES	−75.37	−126.32	−0.74	−0.73	30.09
Constant Forcing					
EC-EARTH	−39.72	−51.60	−0.62	−0.48	117.02
HadGEM2	−45.21	−21.86	−0.73	−0.21	117.60
HadGEM3	−77.93	−15.50	−0.81	−0.09	168.46
IPSL	−6.69	−17.33	−0.24	−0.37	69.04
CNRM	−17.98	−48.70	−0.36	−0.58	106.02
MIROC	−105.42	−9.71	−0.95	−0.05	115.07
M.E.M.	**−48.72**	**−27.67**	**−0.92**	**−0.31**	**46.33**
Stochastic Forcing					
EC-EARTH	−27.51	−68.10	−0.47	−0.69	97.09
HadGEM2	−40.32	8.03	−0.66	0.08	134.67
HadGEM3	−94.63	−36.97	−0.90	−0.21	131.67
IPSL	−9.14	−17.85	−0.41	−0.47	49.57
CNRM	−49.24	−33.87	−0.74	−0.30	118.62
MIROC	−111.82	117.35	−1.01	0.62	109.41
M.E.M.	**−22.86**	**−58.16**	**−0.36**	**−0.53**	**142.04**

Table A4. Same as Table 1 Except for the z_b Patterns

Model	b_1 (m K^{-1})	B_2 (m(g kg^{-1})$^{-1}$)	B_1	B_2	ε (m)
DALES	−73.73	−138.60	−0.70	−0.78	34.30
Constant Forcing					
EC-EARTH	−22.08	−38.22	−0.55	−0.56	72.72
HadGEM2	−16.26	−10.27	−0.67	−0.25	48.97
HadGEM3	−25.59	−28.32	−0.73	−0.45	49.35
IPSL	−3.69	−11.95	−0.17	−0.33	56.40
CNRM	−2.18	−0.39	−0.09	−0.01	65.95
MIROC	−31.09	−20.33	−0.79	−0.30	63.82
M.E.M.	**−15.95**	**−19.26**	**−0.78**	**−0.55**	**21.39**
Stochastic Forcing					
EC-EARTH	62.92	73.55	0.09	0.06	205.28
HadGEM2	−15.91	−7.26	−0.76	−0.20	37.90
HadGEM3	−29.42	−31.71	−0.78	−0.50	43.95
IPSL	−5.06	−11.99	−0.32	−0.44	37.94
CNRM	−10.52	20.39	−0.19	0.22	146.32
MIROC	−6.25	−43.70	−0.24	−1.00	9.41
M.E.M.	**3.09**	**−4.83**	**0.03**	**−0.02**	**339.40**

Table A5. Same as Table 1 Except for the $\langle q_t \rangle$ Patterns

Model	b_1 (g kg^{-1}K^{-1})	b_2	B_1	B_2	ε (g kg^{-1})
DALES	0.23	0.55	0.63	0.87	0.05
Constant Forcing					
EC-EARTH	0.09	0.29	0.44	0.87	0.19
HadGEM2	0.08	0.23	0.43	0.74	0.28
HadGEM3	0.23	0.15	0.73	0.28	0.58
IPSL	0.04	0.22	0.26	0.94	0.13
CNRM	0.05	0.39	0.21	0.97	0.20
MIROC	0.18	0.18	0.86	0.50	0.16
M.E.M.	**0.11**	**0.25**	**0.61**	**0.81**	**0.12**
Stochastic Forcing					
EC-EARTH	0.07	0.31	0.38	0.93	0.15
HadGEM2	0.06	0.19	0.37	0.68	0.29
HadGEM3	0.29	0.19	0.85	0.33	0.44
IPSL	0.03	0.20	0.28	0.99	0.06
CNRM	0.09	0.34	0.40	0.86	0.27
MIROC	0.28	0.10	0.96	0.21	0.23
M.E.M.	**0.14**	**0.23**	**0.73**	**0.67**	**0.11**

Table A6. Same as Table 1 Except for the $\langle \theta_l \rangle$ Patterns

Model	b_1	b_2 (K(g kg^{-1})$^{-1}$)	B_1	B_2	ε (K)
DALES	−0.03	−0.06	−0.68	−0.79	0.02
Constant Forcing					
EC-EARTH	−0.06	0.10	−0.38	0.37	0.41
HadGEM2	−0.09	0.05	−0.55	0.17	0.40
HadGEM3	0.03	−0.05	0.20	−0.19	0.39
IPSL	0.03	0.20	0.16	0.72	0.34
CNRM	0.05	0.32	0.19	0.72	0.52
MIROC	−0.07	0.19	−0.34	0.55	0.46
M.E.M.	**−0.03**	**0.15**	**−0.24**	**0.80**	**0.19**
Stochastic Forcing					
EC-EARTH	−0.02	0.06	−0.16	0.28	0.34
HadGEM2	−0.08	0.02	−0.42	0.07	0.49
HadGEM3	0.09	−0.05	0.67	−0.23	0.27
IPSL	0.00	0.17	0.03	0.70	0.31
CNRM	−0.05	0.29	−0.16	0.52	0.78
MIROC	−0.05	0.21	−0.24	0.56	0.51
M.E.M.	**−0.03**	**0.13**	**−0.24**	**0.70**	**0.22**

Table A7. Same as Table 1 Except for the LHF Patterns

Model	b_1 (W m^{-2} K^{-1})	b_2 (W m^{-2}(g kg^{-1})$^{-1}$)	B_1	B_2	ε (W m^{-2})
DALES	0.43	−6.58	0.12	−1.14	0.60
Constant Forcing					
EC-EARTH	−1.07	−6.82	−0.26	−0.98	2.67
HadGEM2	−1.09	−3.98	−0.31	−0.67	6.87
HadGEM3	−3.58	−2.34	−0.65	−0.25	11.27
IPSL	−0.72	−4.76	−0.26	−1.01	1.09
CNRM	−0.90	−7.77	−0.19	−0.96	4.71
MIROC	−3.82	−4.06	−0.82	−0.51	4.62
M.E.M.	**−1.15**	**−3.29**	**−0.45**	**−0.76**	**3.79**
Stochastic Forcing					
EC-EARTH	−0.88	−6.84	−0.22	−0.99	3.00
HadGEM2	−0.80	−2.12	−0.24	−0.37	8.62
HadGEM3	−4.91	−3.01	−0.83	−0.29	8.54
IPSL	−0.66	−4.47	−0.26	−1.02	0.40
CNRM	−1.56	−6.50	−0.34	−0.84	6.44
MIROC	−1.12	−7.34	−0.26	−0.99	1.39
M.E.M.	**−0.07**	**−4.77**	**−0.02**	**−0.82**	**5.93**

Table A8. Same as Table 1 Except for the SHF Patterns

Model	b_1 (W m^{-2} K^{-1})	b_2 (W m^{-2}(g kg^{-1})$^{-1}$)	B_1	B_2	ε (W m^{-2})
DALES	0.24	−0.16	0.91	−0.34	0.16
Constant Forcing					
EC-EARTH	0.44	−0.76	0.35	−0.36	3.11
HadGEM2	0.92	−0.86	0.74	−0.41	2.30
HadGEM3	−0.31	0.15	−0.29	0.087	2.87
IPSL	−0.26	−1.72	−0.19	−0.75	2.59
CNRM	−0.25	−2.20	−0.15	−0.77	3.17
MIROC	−0.16	−0.25	−0.25	−0.24	1.69
M.E.M.	**−0.04**	**−0.77**	**−0.06**	**−0.75**	**1.17**
Stochastic Forcing					
EC-EARTH	0.14	−0.61	0.15	−0.37	2.49
HadGEM2	0.95	−0.46	0.69	−0.19	2.93
HadGEM3	−0.73	0.23	−0.73	0.13	2.01
IPSL	−0.07	−1.49	−0.05	−0.73	2.48
CNRM	0.57	−2.00	0.27	−0.57	4.66
MIROC	−0.23	−0.82	−0.42	−0.89	0.26
M.E.M.	**0.16**	**−0.82**	**0.22**	**−0.64**	**1.60**

References

Bellon, G., and B. Stevens (2012), Using the sensitivity of large-eddy simulations to evaluate atmospheric-boundary-layer models, *J. Atmos. Sci.*, 69, 1582–1601.

Blossey, P. N., C. S. Bretherton, M. Zhang, A. Cheng, S. Endo, T. Heus, Y. Liu, A. Lock, S. R. de Roode, and K.-M. Xu (2013), Marine low cloud sensitivity to an idealized climate change: The CGILS LES intercomparison, *J. Adv. Model. Earth Syst.*, 5, 234–258, doi:10.1002/jame.20025.

Böing, S. J., H. J. J. Jonker, A. P. Siebesma, and W. W. Grabowski (2012), Influence of the subcloud layer on the development of a deep convective ensemble, *J. Atmos. Sci.*, 69(9), 2682–2698.

Bony, S., and J.-L. Dufresne (2005), Marine boundary layer clouds at the heart of tropical cloud feedback uncertainties in climate models, *Geophys. Res. Lett.*, 32, L20806, doi:10.1029/2005GL023851.

Bony, S., and K. A. Emanuel (2001), A parameterization of the cloudiness associated with cumulus convection; evaluation using TOGA COARE data, *J. Atmos. Sci.*, 58(21), 3158–3183.

Boutle, I. A., and S. J. Abel (2012), Microphysical controls on the stratocumulus topped boundary-layer structure during VOCALS-REx, *Atmos. Chem. Phys.*, 12(6), 2849–2863.

Bretherton, C. S., and M. C. Wyant (1997), Moisture transport, lower-tropospheric stability, and decoupling of cloud-topped boundary layers, *J. Atmos. Sci.*, 54(1), 148–167.

Bretherton, C. S., P. N. Blossey, and C. R. Jones (2013), Mechanisms of marine low cloud sensitivity to idealized climate perturbations: A single-LES exploration extending the CGILS cases, *J. Adv. Model. Earth Syst.*, 5, 316–337, doi:10.1002/jame.20019.

Brient, F., and S. Bony (2012), Interpretation of the positive low-cloud feedback predicted by a climate model under global warming, *Clim. Dyn.*, 40, 1–17.

Cess, R. D., et al. (1989), Interpretation of cloud-climate feedback as produced by 14 atmospheric general circulation models, *Science*, 245(4917), 513–516.

Cheedela, S. K. (2013), Single column models and low cloud feedbacks, PhD thesis, Univ. of Hamburg, Hamburg, Germany.

Dal Gesso, S., A. P. Siebesma, R. S. de Roode, and J. M. van Wessem (2014a), A mixed-layer model perspective on stratocumulus steady-states in a perturbed climate, *Q. J. R. Meteorol. Soc.*, *140*(684), 2119–2131.

Dal Gesso, S., A. P. Siebesma, and de Roode (2014b), Evaluation of low-cloud climate feedback through single-column model equilibrium states, *Q. J. R. Meteorol. Soc.*

Deardorff, J. W. (1966), The counter-gradient heat flux in the lower atmosphere and in the laboratory, *J. Atmos. Sci.*, *23*(5), 503–506.

Duynkerke, P. G., et al. (2004), Observations and numerical simulations of the diurnal cycle of the EUROCS stratocumulus case, *Q. J. R. Meteorol. Soc.*, *130*(604), 3269–3296.

Emanuel, K. A. (1991), A scheme for representing cumulus convection in large-scale models, *J. Atmos. Sci.*, *48*(21), 2313–2329.

Grant, A. L. M. (2001), Cloud-base fluxes in the cumulus-capped boundary layer, *Q. J. R. Meteorol. Soc.*, *127*(572), 407–421.

Hazeleger, W., et al. (2012), EC-Earth V2. 2: Description and validation of a new seamless earth system prediction model, *Clim. Dyn.*, *39*(11), 2611–2629.

Heus, T., et al. (2010), Formulation of the Dutch atmospheric large-eddy simulation (DALES) and overview of its applications, *Geosci. Model Dev.*, *3*(2), 415–444.

Hourdin, F., et al. (2006), The LMDZ4 general circulation model: Climate performance and sensitivity to parameterized physics with emphasis on tropical convection, *Clim. Dyn.*, *27*(7–8), 787–813.

Kessler, E. (1995), On the continuity and distribution of water substance in atmospheric circulations, *Atmos. Res.*, *38*(1), 109–145.

Klein, S. A., and D. L. Hartmann (1993), The seasonal cycle of low stratiform clouds, *J. Clim.*, *6*(8), 1587–1606.

Lenderink, G., and A. A. M. Holtslag (2000), Evaluation of the kinetic energy approach for modeling turbulent fluxes in stratocumulus, *Mon. Weather Rev.*, *128*(1), 244–258.

Lin, J.-L., T. Qian, and T. Shinoda (2014), Stratocumulus clouds in southeastern pacific simulated by eight CMIP5/CFMIP global climate models, *J. Clim.*, *27*(8), 3000–3022.

Lock, A. P., A. R. Brown, M. R. Bush, G. M. Martin, and R. N. B. Smith (2000), A new boundary layer mixing scheme. Part I: Scheme description and single-column model tests, *Mon. Weather Rev.*, *128*(9), 3187–3199.

Martin, G. M., et al. (2011), The HadGEM2 family of met office unified model climate configurations, *Geosci. Model Dev. Discuss.*, *4*(2), 765–841.

Mellor, G. L., and T. Yamada (1974), A hierarchy of turbulence closure models for planetary boundary layers, *J. Atmos. Sci.*, *31*(7), 1791–1806.

Nakanishi, M., and H. Niino (2004), An improved Mellor–Yamada level-3 model with condensation physics: Its design and verification, *Boundary Layer Meteorol.*, *112*(1), 1–31.

Nam, C., S. Bony, J.-L. Dufresne, and H. Chepfer (2012), The too few, too bright tropical low-cloud problem in CMIP5 models, *Geophys. Res. Lett.*, *39*, L21801, doi:10.1029/2012GL053421.

Park, S., C. B. Leovy, and M. A. Rozendaal (2004), A new heuristic Lagrangian marine boundary layer cloud model, *J. Atmos. Sci.*, *61*(24), 3002–3024.

Qu, X., A. Hall, S. A. Klein, and P. M. Caldwell (2013), On the spread of changes in marine low cloud cover in climate model simulations of the 21st century, *Clim. Dyn.*, *42*, 1–24.

Randall, D. A., J. A. Coakley Jr., D. H. Lenschow, C. W. Fairall, and R. A. Kropfli (1984), Outlook for research on subtropical marine stratification clouds, *Bull. Am. Meteorol. Soc.*, *65*(12), 1290–1301.

Ricard, J., and J. Royer (1993), A statistical cloud scheme for use in an AGCM, *Ann. Geophys.*, *11*, 1095–1115.

Rieck, M., L. Nuijens, and B. Stevens (2012), Marine boundary layer cloud feedbacks in a constant relative humidity atmosphere, *J. Atmos. Sci.*, *69*(8), 2538–2550.

Siebesma, A. P., et al. (2004), Cloud representation in general-circulation models over the northern Pacific Ocean: A EUROCS intercomparison study, *Q. J. R. Meteorol. Soc.*, *130*(604), 3245–3267.

Siebesma, A. P., P. M. M. Soares, and J. Teixeira (2007), A combined eddy-diffusivity mass-flux approach for the convective boundary layer, *J. Atmos. Sci.*, *64*(4), 1230–1248.

Smith, R. N. B. (1990), A scheme for predicting layer clouds and their water content in a general circulation model, *Q. J. R. Meteorol. Soc.*, *116*(492), 435–460.

Taylor, K. E., R. J. Stouffer, and G. A. Meehl (2012), An overview of CMIP5 and the experiment design, *Bull. Am. Meteorol. Soc.*, *93*(4), 485–498.

Teixeira, J., et al. (2011), Tropical and subtropical cloud transitions in weather and climate prediction models: The GCSS/WGNE pacific cross-section intercomparison (GPCI), *J. Clim.*, *24*(20), 5223–5256.

Tiedtke, M. (1989), A comprehensive mass flux scheme for cumulus parameterization in large-scale models, *Mon. Weather Rev.*, *117*(8), 1779–1800.

Tiedtke, M. (1993), Representation of clouds in large-scale models, *Mon. Weather Rev.*, *121*(11), 3040–3061.

van der Dussen, J. J., S. R. de Roode, S. Dal Gesso, and A. P. Siebesma (2014), A LES study of the influence of the free troposphere on the response of stratocumulus response to a climate perturbation, *J. Adv. Model. Earth Syst*, in press.

Vecchi, G. A., B. J. Soden, A. T. Wittenberg, I. M. Held, A. Leetmaa, and M. J. Harrison (2006), Weakening of tropical pacific atmospheric circulation due to anthropogenic forcing, *Nature*, *441*(7089), 73–76.

Vial, J., J.-L. Dufresne, and S. Bony (2013), On the interpretation of inter-model spread in CMIP5 climate sensitivity estimates, *Clim. Dyn.*, *41*(11–12), 3339–3362.

Voldoire, A., et al. (2013), The CNRM-CM5.1 global climate model: Description and basic evaluation, *Clim. Dyn.*, *40*(9–10), 2091–2121.

Walters, D. N., et al. (2011), The met office unified model global atmosphere 3.0/3.1 and JULES global land 3.0/3.1 configurations, *Geosci. Model Dev. Discuss.*, *4*(2), 1213–1271.

Watanabe, M., S. Emori, M. Satoh, and H. Miura (2009), A PDF-based hybrid prognostic cloud scheme for general circulation models, *Clim. Dyn.*, *33*(6), 795–816.

Watanabe, M., et al. (2010), Improved climate simulation by MIROC5: Mean states, variability, and climate sensitivity, *J. Clim.*, *23*, 6312–6335.

Webb, M., C. Senior, S. Bony, and J.-J. Morcrette (2001), Combining ERBE and ISCCP data to assess clouds in the Hadley centre, ECMWF and LMD atmospheric climate models, *Clim. Dyn.*, *17*(12), 905–922.

Williams, K. D., and M. J. Webb (2009), A quantitative performance assessment of cloud regimes in climate models, *Clim. Dyn.*, *33*(1), 141–157.

Wilson, D. R., and S. P. Ballard (1999), A microphysically based precipitation scheme for the UK Meteorological Office Unified Model, *Q. J. R. Meteorol. Soc.*, *125*(557), 1607–1636.

Wilson, D. R., A. C. Bushell, A. M. Kerr-Munslow, J. D. Price, and C. J. Morcrette (2008), PC2: A prognostic cloud fraction and condensation scheme. I: Scheme description, _Q. J. R. Meteorol. Soc._, _134_(637), 2093–2107.

Wood, R. (2012), Stratocumulus clouds, _Mon. Weather Rev._, _140_(8), 2373–2423.

Wood, R., and C. S. Bretherton (2004), Boundary layer depth, entrainment, and decoupling in the cloud-capped subtropical and tropical marine boundary layer, _J. Clim._, _17_(18), 3576–3588.

Zhang, M., and C. S. Bretherton (2008), Mechanisms of low cloud-climate feedback in idealized single-column simulations with the community atmospheric model, version 3 (CAM3), _J. Clim._, _21_(18), 4859–4878.

Zhang, M., et al. (2013), CGILS: Results from the first phase of an international project to understand the physical mechanisms of low cloud feedbacks in single column models, _J. Adv. Model. Earth Syst._, _5_, 826–842, doi:10.1002/2013MS000246.